AIMS Mathematics, 10(8): 17832–17867.
DOI: 10.3934/math.2025795
Received: 26 April 2025
Revised: 19 July 2025
Accepted: 22 July 2025
Published: 06 August 2025

https://www.aimspress.com/journal/Math

Research article

A non-perturbative methodology for a cantilever-beam dynamical system with bifurcation and negative derivative feedback controlling

Asma Alanazy[1], A.T. EL-Sayed[2,*] and F. T. El-Bahrawy[2]

[1] Department of Mathematics, Faculty of Science, Northern Border University, Arar 1321, Kingdom of Saudi Arabia
[2] Basic Science Department, Modern Academy for Engineering and Technology, Elmokattam, Cairo 11439, Egypt

* **Correspondence:** Email: ashraftaha211@yahoo.com, atelsayed@eng.modern-academy.edu.eg.

Abstract: The existence study explored a cantilever-beam dynamical system with bifurcation and negative derivative feedback to understand and regulate nonlinear phenomena in flexible constructions, improving stability and performance in engineering applications. The nonlinear transverse vibrations of a cantilever beam mechanism were investigated under initial resonance conditions. A detailed clarification of the non-perturbative method (NPM) was presented to introduce a novel approach in handling nonlinearities systems. Simply, NPM transformed the weakly nonlinear oscillator into an equivalent linear differential equation (ODE). The theoretical results obtained through NPM were validated using numerical simulations in MATLAB. Moreover, NPM facilitated the stability analysis of the system, which was not previously attainable via traditional approaches. Significantly, NPM resolved limitations encountered in previous methods, offering a more strong solution framework. The system was completely different in the second part of the study, since it only had two degrees of freedom (2DOF) controlled through an individual input. The study outlined the bifurcation and control strategy of the 2DOF's response vibrations. Negative derivative feedback (NDF) was used to control the system's operation to minimize the harmful vibrations it produced. To identify several bifurcations inside the system, bifurcation characterization was conducted on an examined figure, considering two varied values of the controller gain. The fundamental objective of this study was to explore the transformation of nonlinear ODEs into linear ones and assess the efficacy of the control approach and bifurcation analysis in stabilizing cantilever beams. The multiple time-scales method (MTSM) was utilized for analyzing the controlled linear equivalent algorithm. Several diagrams illustrated the prototype's sturdy construction. To mitigate damaging vibrations in the system, the NDF was

recommended. Predicted solutions were validated through numerical simulations using the fourth-order Runge-Kutta method (RK4), demonstrating an excellent correlation. The stability and steady-state amplitude of nonlinear patterns were analyzed both before and after applying control. Additionally, frequency response curves (FRCs) and optimal system configurations were evaluated under various controller and system parameter settings.

Keywords: nonlinear oscillations; bifurcation**;** Poincaré map**;** multiple time-scale method; stability analysis; NDF controller; non-perturbative method
Mathematics Subject Classification: 34A34, 37N35, 70J99, 70K20, 74H10

1. Introduction

As shown in Figure 1, a beam is an intrinsic part intended of bearing transverse loads that act perpendicular to its investigation longitudinal axis. The nonlinear behavior of various engineering structures such as large space structures, chopper propeller blades, solar power plant blades, flying wings, arm-type deployment mechanisms, slider-crank networks, and mechanical building materials are commonly modeled via implementing a cantilever beam structure (CBS). Nonlinear vibrations in geometrical engineering systems are caused only by the system's nonlinear properties and external excitation forces. Negligible systemic nonlinearities are occasionally achievable when these systems are activated with small excitation amplitudes distant from their resonance conditions.

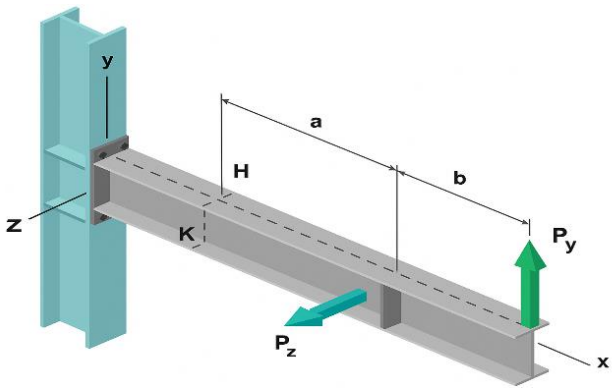

Figure 1. Sketch of a cantilever beam visual representation model.

In contrast, nonlinear ODEs are frequently believed to have approximate solutions using a variety of perturbation approaches; on the other hand, linear ODEs are easily solved using well-established techniques. Furthermore, most vibration problems have nonlinear properties; an increasing number of scientists are interested in analyzing nonlinear oscillations. Nonlinear ODEs are essential in understanding various scientific and technical processes, as many real-world phenomena exhibit nonlinear behavior. In applied mathematics, physics, and engineering, nonlinear ODEs play a crucial role [1]. It is vital to emphasize the importance of mathematical calculations in many studies in applied sciences and technological disciplines that address nonlinear ODEs [2]. In literature, various approximate analytical techniques, in analyzing nonlinear ODEs, are utilized to establish how

amplitudes and frequencies relate to one another in nonlinear oscillators. Among these, the perturbation method is the most adaptable approach in analyzing nonlinear engineering problems. It is frequently used to get rough analytical responses to nonlinear ODEs [3]. Several novel techniques are recently developed of the analytical solution of nonlinear ODEs [4–7]. The Lindstedt-Poincaré technique was used to analyze such problems [8]. These techniques include the homotopy perturbation method (HPM) [9]. In addition to developing the frequency formula, a novel method of addressing linearity in a nonlinear equation was devised [10–12]. The findings indicate that the approach yields highly accurate results. Using a slightly refined technique, the experiment confirmed efficacy in quickly determining the amplitude-frequency relationship of a nonlinear oscillator. Developmental micro-electro-mechanical devices and packaging solutions were simulated using the frequency-amplitude relationship in nonlinear vibrating structures [13]. A useful strategy in comprehending the vibration properties of nonlinear systems is created by putting forth a straightforward frequency prediction method for nonlinear oscillators with different initial conditions. In the following points, some summarized advantages of NPM are reported:

1) An innovative approach is employed to derive a new linear ODE that is equivalent to the original nonlinear one.
2) In light of the new method, there is an accurate link between these two ODEs.
3) A new linear ODE is equivalent to the old nonlinear one and is created using the creative method. The shortcomings of earlier techniques are successfully addressed by this strategy.
4) Unlike other perturbation approaches, the NPM allows, simply, experts to assess the problem's stability examination.
5) One of the approaches appears to be a straightforward, promising, and interesting tool.
6) The NPM may be expanded to encompass other combinations of connected dynamical systems deemed significant, efficient, and persuasive.
7) The Taylor expansion is utilized to aid in the computation of these restoring forces across all perturbation methods, including the foundational approach known as multiple time scale. Moreover, the NPM overlooked this deficiency.
8) The NPM utilizes a unique methodology for addressing restoring forces, distinct from the traditional perturbation approach; it is not categorized as a perturbation technique.

After introducing and demonstrating the fundamental frequency formulation of nonlinear oscillators, a modification was proposed [14]. Both conceptual and experimentally, efforts were made to suppress oscillations in a flexible cantilever beam [15]. The nonlinear vibrations of the micro-beam are examined for two distinct resonance scenarios, super-harmonic and harmonic resonances, using the MTSM. After introducing and demonstrating the fundamental frequency formulation for nonlinear oscillators, a modification was proposed [16]. This study clearly demonstrated that the boundary conditions significantly influence the micro-beams' vibrations [17]. When an external excitation force is applied to a smooth yet discontinuous oscillator, the NDF controller is employed to manage the oscillations [18]. An approximate solution of the vibrating system was constructed using the MTSM. The algorithm's stability was analyzed utilizing FRCs, and the effect of every system parameter was assessed via numerical calculations [19]. It is pointed out that the use of a resonant control technique called the NDF controller is used to operate a quarter-vehicle car and is subjected to primary parametric stimulation. This control technique is efficient and successful since it avoids dangerous vibrations. This control is effective and efficient, as it prevents harmful vibrations during operation. Consequently, the NDF controller is considered to be fundamental in this application. Moreover, for the first time,

the resilience of a quarter-vehicle automotive system to variations in its natural frequency has been examined. A simple procedure is described for the ideal NDF controller configuration that achieves maximum damping and H2 optimization. This filtering capability enables it to efficiently mitigate both higher and lower frequency disturbances, making it suitable for high-performance vibration mitigation applications [20].

Based on performance measures, it was demonstrated that the NDF controller performs better than the positive position feedback (PPF) controller. A result-based feedback control approach was used to create and implement an adaptive NDF modal control algorithm on a carbon fiber plate, as previously shown [21]. To reduce undesirable vibrations, these diverse controls can be used on a variety of constructions. Several studies [22–28] were employed piezoelectric patches with different distributions to reduce vibrations in conical shells. Numerous researchers developed a variety of techniques for this purpose [29]. The main drawback of this approach is that the reduction in vibration amplitude is minimal. Consequently, active techniques for mitigating structural vibrations are preferred. The integral resonant negative derivative feedback (IRNDF) controller, a revolutionary control technique, was used to minimize the impact of vibration of a double van der Pol oscillator under external excitations was examined [30]. The proportional (P), proportional-integral (PI), and proportional-integral-derivative (PID) controller types were demonstrated to control the torsional vibration behavior of a dynamical system; they used PID control. Seeing the effects of P and PI control, the PID controller sought to improve system stability [31]. The MTSM was implemented to figure out the controlled system analytically. The system's steady-state response and stability under primary resonance circumstances ($\Omega_1 \cong \omega_1, \Omega_2 \cong \omega_2$) resonance phenomena, particularly the most severe types, are addressed using the FRC. The chaotic behavior of the nonlinear dynamical system is investigated alongside numerical solutions for various parameter values [32]. We implement the MTSM up to the second-order estimation to arrive at analytical results. The FRCs is employed to examine and suppress synchronous primary and internal resonance conditions in order to assess system stability. For all calculations, MATLAB and Maple were executed [33]. The stability of coupled multiple pendulums under the influence external harmonic excitation was outlined [34]. The achievements of computerized simulation are exposed as multicolored maps of the maximal Lyapunov exponent (LE) using a mathematical model. Furthermore, diagrammatic depictions of the mathematical arrangements of the attractors on Poincaré cross sections and maps show the density of trajectory points over a control plane are presented. The monoclinic and sub-harmonic bifurcation boundaries were determined using the Melnikov and averaging techniques [35]. Discrete implicit maps were employed to study the bifurcation of trees of periodic motions in a parametrically excited pendulum [36]. For periodic motions in such a system, mapping structures are constructed from these discrete maps. The nonlinear algebraic equations, derived from the implicit maps, are used to generate analytical bifurcation trees, illustrate the transition from periodic motions to chaos. Finally, the bifurcation and associated stability of these periodic motions were analyzed.

The practical applications of cantilever-beam systems, incorporating bifurcation analysis and NDF control, are particularly significant in sophisticated smart structures and adaptive systems. In smart materials and structures, including adaptable aircraft components, vibration-sensitive buildings, and precision manufacturing tools, regulating dynamic reactions via feedback systems facilitates real-time adjustments to external disturbances or internal variations. This is crucial in settings where instability-induced failure may result in disastrous outcomes or expensive interruptions. In electromechanical systems and nanoscale devices, where cantilever beams serve as sensors and

actuators, regulating bifurcations is essential in sustaining functioning under fluctuating loads and improving signal clarity. In biomedical engineering, micro-scale cantilever beams are employed in diagnostic equipment, with feedback control guaranteeing precision and consistency in data. The experimental investigation of these systems establishes a basis in creating control algorithms that are resilient, scalable, and relevant to nonlinear systems beyond basic beams, hence enhancing safety, adaptability, and efficiency across several industries.

2. A rapid overview of NPM

Examine a weakly nonlinear oscillator as ODE of the following type that is extremely nonlinear up to the third order:

$$\zeta'' + F(\zeta, \zeta', \zeta'') + G(\zeta, \zeta', \zeta'') = H(\zeta, \zeta', \zeta''), \tag{1}$$

where each$F(\zeta, \zeta', \zeta'')$and $G(\zeta, \zeta', \zeta'')$are odd functions. As is well-known, these functions produce secular terms [1, 3]. At the same time,$H(\zeta, \zeta', \zeta'')$ is a quadratic function. Overall, up to the third-order, these functions may typically formulate as follows:

$$\left.\begin{aligned} F(\zeta, \zeta', \zeta'') &= m_1\zeta' + n_1\zeta\zeta'\zeta'' + p_1\zeta^2\zeta'^2 + q_1\zeta'^3 + s_1\zeta''^2\zeta' \\ G(\zeta, \zeta', \zeta'') &= \omega^2\zeta + q_2\zeta^3 + p_2\zeta\zeta'^2 + s_2\zeta''\zeta'^2 \\ H(\zeta, \zeta', \zeta'') &= m_3\zeta\zeta' + n_3\zeta'^2 + p_3\zeta^2 + q_3\zeta''\zeta' + s_3\zeta\zeta'' \end{aligned}\right\}, \tag{2}$$

where $m_k, n_k, p_k, q_k, s_k (k = 1,2,3)$ are coefficients that remain constant., and ω symbolizes the structure's natural frequency.

As is well- known, the primary objective of the NPM is to derive an alternative linear ODE. To generate this ODE, three constants will be determined.

It should be noted that He's frequency formula (HFF) is crucial in converting a weakly nonlinear oscillator of ODE into linear-like representations by offering an analytical approximation of the frequency of nonlinear oscillators without the necessity of solving the complete problem. This approach facilitates the analysis of extremely nonlinear systems by approximating their behavior with a frequency contingent upon the system's amplitude. This action efficiently linearizes the system's reaction, facilitating comprehension and prediction of its dynamics. This approach avoids the restrictions of conventional perturbation techniques, delivering precise solutions of substantial nonlinearities and yielding significant insights into the system's periodic dynamics with the smallest computer resources. Additionally, the uniqueness of the present research relates to the consequences of NPM. It is widely recognized that weakly nonlinear oscillator of ODEs lack compact solutions; hence, perturbation techniques are crucial for their study. As is well-known, all standard perturbation methods, including the MTSM, is to be complex in their procedures. Consequently, NPM represents a novel approach to tackling these intricate challenges. Moreover, in contrast to all traditional methods, the NPM refrains from utilizing Taylor expansion of trigonometric functions. The examination of NPM is quite uncomplicated. Furthermore, as previously mentioned, a flowchart depicting the methodological approach will be incorporated to improve reader understanding. As we previously said, the NPM is completely different from all perturbation techniques. Therefore, no comparison between the other methods is made. On the other side, the NPM produces coupled linear ODEs that are comparable with the given nonlinear ones. Therefore, numerical validations are presented to the

effeteness of the NPM and to produce very small absolute error. It should be noticed that Moatimid et al. [37–42] was previously adopted the NPM for a different situation in the topic of the dynamical systems. Notably, the purpose of constructing a linear ODE is to replicate the behavior of simple harmonic motion to achieve this goal. As per He [10], a guessing solution of the provided nonlinear ODE is as follows [10]:

$$z = A\cos\Omega\, t. \tag{3}$$

The following are the initial conditions (ICs): $z(0) = A$, and $z^{'}(0) = A$.

The total frequency, which will be ascertained later, is captured by the parameterΩ. Below provides the necessary linear differential equation:

$$z^{''} + \sigma_{eqv} z^{'} + \omega_{eqv}^2 z = \Gamma. \tag{4}$$

The three criteria can be assessed in the manner described below, as demonstrated before [37–42]:

$$\sigma_{eqv} = \frac{\int_0^{2\pi/\Omega} z^{'} F(z,z^{'},z^{''})dt}{\int_0^{2\pi/\Omega} z^{'2} dt} = \sigma_{eqv}(\Omega). \tag{5}$$

Think about a similar frequency. ω_{eqv}^2, which can be computed using the following function and the overall frequency:

$$\omega_{eqv}^2 = \frac{\int_0^{2\pi/\Omega} zG(z,z^{'},z^{''})dt}{\int_0^{2\pi/\Omega} z^2 dt} = \omega_{eqv}^2(\Omega). \tag{6}$$

It should be noted that the quadratic formula is a part of the non-secular section.

Consequently, the inhomogeneity will be calculated by substituting: $\zeta \to EA, \zeta' \to EA\Omega$, and $\zeta'' \to EA\Omega^2$, even in the non-secular function $H(\zeta, \zeta', \zeta'')$. As previously shown [37–42], the parameter $E$is defined as$E = 1/2\sqrt{n-r}$, where n demonstrates the system's order and $r$represents the system's level of freedom. Consequently, in this instance, one receives$n = 2$and, $r = 1$, then the value of$E = 1/2$. It corresponds to the quadratic's (non-secular terms) value. Consequently, the inhomogeneity component will be calculated by substituting: $\zeta \to \frac{A}{2}$, $\zeta' \to \frac{A\Omega}{2}$, and $\zeta'' \to \frac{A\Omega^2}{2}$.

The following substitution can be used to express Eq (4) in the ordinary normal form for simplicity's sake:

$$z(t) = f(t)Exp(-\sigma_{eqv}t/2). \tag{7}$$

Actually, to convert the linear ODE as given in Eq (4) into a simple harmonic motion, the middle term in Eq (4) should be removed. This process is simply obtainable via the standard normal form as shown in Eq (7).

When Eq (7) is entered into Eq (4), it produces

$$f^{''} + \left(\omega_{eqv}^2 - \frac{1}{4}\sigma_{eqv}^2\right) f = \Gamma Exp(-\sigma_{eqv}t/2). \tag{8}$$

Lastly, the total frequency is stated as $\Omega^2 = \omega_{eqv}^2 - \frac{1}{4}\sigma_{eqv}^2$.

The NPM technique is delineated in the subsequent step-by-step flowchart to improve clarity and comprehension. This visual guide delineates the technique, highlighting the critical procedures that streamline and enhance the problem-solving approach. Consequently, Figure 2 presents a comprehensive flowchart that delineates the methodical process employed to analyze a nonlinear ordinary differential equation through the application of the NPM in conjunction with the HFF. The approach is designed to transform a nonlinear ODE into an equivalent linear one, and the facilitating analysis. The conversion is achieved by proposing a trial solution to the nonlinear system. Upon presentation of this solution, it is subjected to stringent testing and validation using numerical simulations.

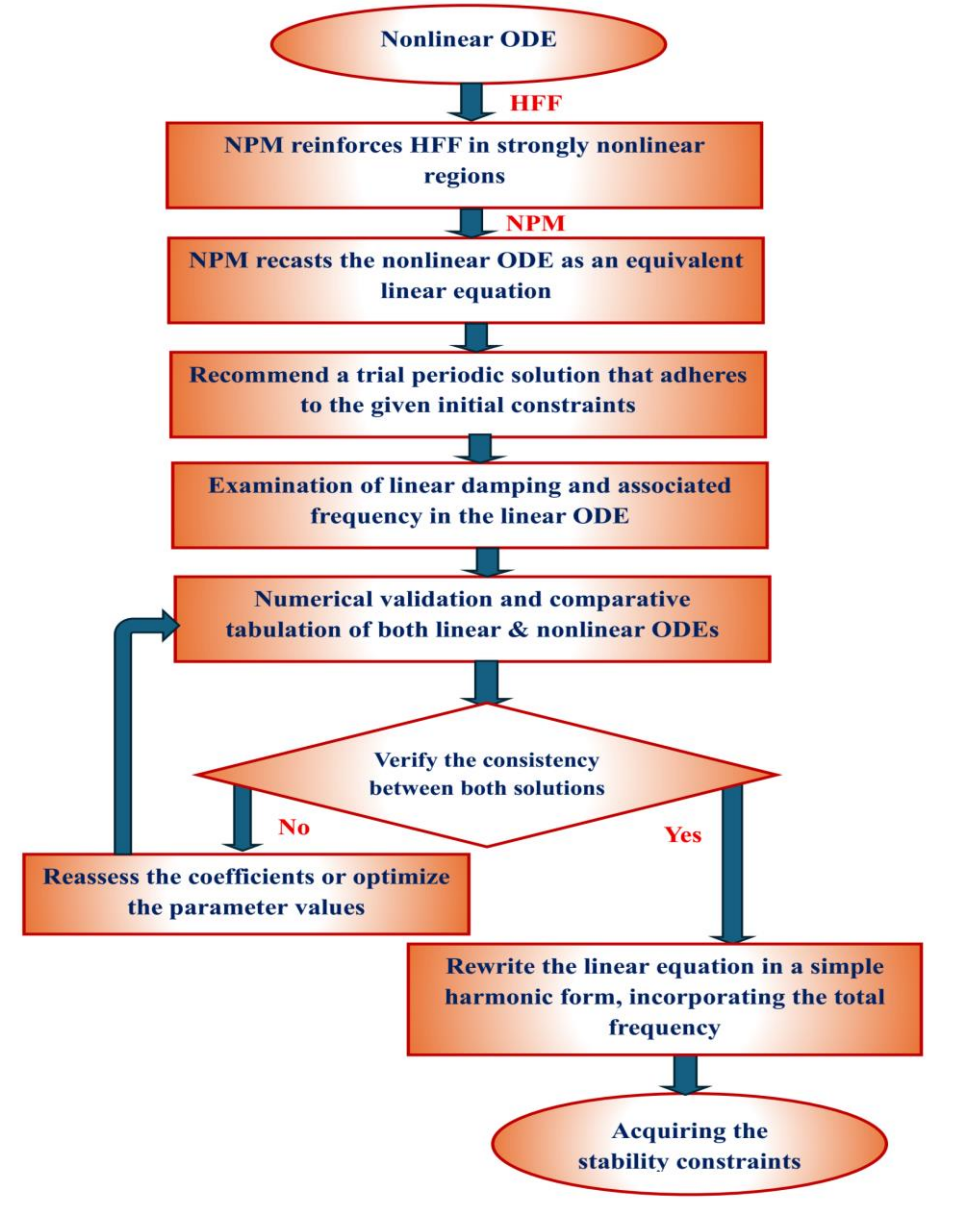

Figure 2. Establishes the process, specifically highlighting the integration of NPM and HFF.

3. The framework's technique without control

In actuality, the shape of the fundamental nonlinear ODE of motion is [43]

$$\ddot{x} + \alpha\dot{x} + \beta_1\dot{x}^3 + \beta_2\dot{x}^5 + \omega^2 x + \gamma_1 x^3 + \gamma_2 x^5 + \delta_1(x\dot{x}^2 + x^2\ddot{x}) + \delta_2(x^3\dot{x}^2 + x^4\ddot{x}) = f\cos\Omega t, \tag{9}$$

where the physical coefficients are addressed as follows:

x is the cantilever beam's displacement, α is the damping coefficient, $\beta_1$and $\beta_2$are coefficients of the nonlinearities, γ_1 and $\gamma_2$are nonlinear terms, ω is the natural frequency, $\delta_1$and $\delta_2$are nonlinear physical quantities, and Ω is the excitation frequency. Additionally, the parameter f denotes the excitation force's amplitude in addition to the original requirements. Also, we can summarize the physical meaning of the terms in Eq. (9) as follows in Table 1.

Table 1. Physical meaning of the term group.

Term group	Physical role
$\alpha\dot{x}$	Ordinary linear damping
$\beta_1\dot{x}^3$, $\beta_2\dot{x}^5$	Cubic/ quintic damping
$\omega^2 x$	Small-deflection stiffness
$\gamma_1 x^3$, $\gamma_2 x^5$	Cubic/ quintic stiffness (softening if $\gamma < 0$) or (hardening if $\gamma > 0$)
δ_1 term	Nonlinear damping-stiffness interaction
δ_2 term	Higher-order interaction
$f\cos\Omega t$	External harmonic excitation force

As usual, the initial conditions (ICs) are written as follows [37–42]:

$$x(0) = A, \text{ and } \dot{x}(0) = 0, \tag{10}$$

Perturbation theory has been central to the study of many nonlinear dynamic systems in recent decades. The natural nonlinearity of these systems arises from the nonlinear behavior of their dynamic components during operation. Traditional linear approaches rely on the assumption that only a limited number of operations are feasible, and these methods may fail when system limits are reached, leading to instability or poor performance. Therefore, it has been proposed to apply perturbation techniques to these nonlinear systems. Such methods not only evaluate the system's stability and performance, but also generate approximate analytical solutions. Currently, there is also a recommendation to analyze nonlinear equations directly, without perturbations, using specialized methods, where the convergence of large series solutions is not a concern. The primary goal of the current investigation is to assess how well linearized approaches approximate the behavior of the nonlinear system. To solve the nonlinear structure, the NPM must generate a trial solution that satisfies the ICs.

One way to characterize the recommendation trial solution would be as follows.

$$u(t) = A\cos\varphi t, \dot{u}(t) = -A\varphi\sin\varphi t, \ddot{u}(t) = -A\varphi^2\cos\varphi t. \tag{11}$$

Now, Eq (9) may be formulated as follows:

$$\ddot{x} + f_1(\ddot{u}) + f_0(u, \dot{u}, \ddot{u}) = F\cos\Omega t, \tag{12}$$

where

$$f_0 = \alpha\dot{x} + \beta_1\dot{x}^3 + \beta_2\dot{x}^5, \tag{13}$$

and

$$f_1 = \omega^2 x + \gamma_1 x^3 + \gamma_2 x^5 + \delta_1(x\dot{x}^2 + x^2\ddot{x}) + \delta_2(x^3\dot{x}^2 + x^4\ddot{x}). \tag{14}$$

Weighted residual improvement is an effective method for estimating the frequency. This frequency estimate can be used to determine the occurrence of unusual terms in the fundamental equation of motion. By applying this approach along with Eq (12), one can approximately determine the frequency, leading to the following conclusion, as previously reported [37–42]:

$$\omega_{eqv}^2 = \frac{\int_0^{2\pi/\varphi} u f_1(u,\dot{u},\ddot{u})dt}{\int_0^{2\pi/\varphi} u^2 dt}. \tag{15}$$

Following the presentation and demonstration of the nonlinear oscillators' abbreviated frequency construction, adaptation was recommended. Using mathematics software, we can simplify the integration result of Eq (6), which is rather challenging. One sorts out

$$\omega_{eqv}^2 = -\frac{1}{2}\delta_2 A^4\varphi^2 + \frac{5}{8}\gamma_2 A^4 + \omega^2 + \frac{3}{4}\gamma_1 A^2 - \frac{1}{2}\delta_1 A^2\varphi^2. \tag{16}$$

Equation (16) represents the equivalent frequency of the associated linear ODE. Similarly, the corresponding equivalent damping can be determined as follows:

$$\mu_{eqv} = \frac{\int_0^{2\pi/\varphi} \dot{u} f_0(\dot{u})dt}{\int_0^{2\pi/\varphi} \dot{u}^2 dt}. \tag{17}$$

As previously shown, we can evaluate the integrations in Eq (17) as follows

$$\mu_{eqv} = \alpha + \frac{5}{8}\beta_2 A^4\varphi^4 + \frac{3}{4}\beta_1 A^2\varphi^2. \tag{18}$$

The associated linear ODE can now be produced as

$$\ddot{u} + \mu_{eqv}\dot{u} + \omega_{eqv}^2 u = F\cos\Omega\, t. \tag{19}$$

Equation (19) can be converted via the standard form in the absence of the excitation force's frequency. ($\Omega \to 0$):

$$u(t) = f(t)e^{-\frac{\mu_{eqv}}{2}t}. \tag{20}$$

Consequently, it is capable of being interpreted as:

$$\ddot{f}(t) + \varphi^2 f = 0, \tag{21}$$

where $\varphi^2 = \omega_{eqv}^2 - \mu_{eqv}^2/4$.

$$\varphi^2 > 0 \text{ and } \mu_{eqv} > 0. \tag{22}$$

3.1. Validation of NPM

For more convenience, to validate the obtained theoretical result, a numerical comparison between Eqs (9) and (19) are graphed for a sample chosen system as follows:

$$\omega = 10; \alpha = 0.16; \beta_1 = 0.3331; \beta_2 = 0.1299; \gamma_1 = 22.5; \gamma_2 = 0.1319;$$

$$\delta_1 = -4.5; \delta_2 = 2.2; f = 0.5; \Omega = 9; A = 0.01.$$

In Figure 3, the numerical solution (NS) of the nonlinear ODE (9) is compared with the solution obtained using the NPM-based linear ODE (19). The close agreement between the two solutions demonstrates the high accuracy and reliability of the proposed NPM. This strong consistency confirms that the outcomes produced by both approaches are dependable and in good agreement. Furthermore, the absolute errors calculated using a MATLAB program are presented and summarized in Table 2.

Table 2. Approves the equivalence between the NS of $x(t)$ and its corresponding NPM $u(t)$.

$Time$	NS for $x(t)$ Nonlinear ODE	NPM for $u(t)$ Linear ODE	Absolute error
0	0.01	0.01	0
5	0.00721157	0.0069361	0.00027547
10	-0.013557	0.0148543	0.0012973
15	-0.0292684	-0.0298563	0.0005879
20	-0.021343	-0.0192598	0.0020832
25	0.00831714	0.0112593	0.00294216
30	0.0253428	0.0254634	0.0001206
35	0.0186569	0.0177555	0.0009014
40	-0.0100171	-0.00708981	0.00292729
45	-0.0256914	-0.0253292	0.0003622
50	-0.0200781	-0.019393	0.0006851

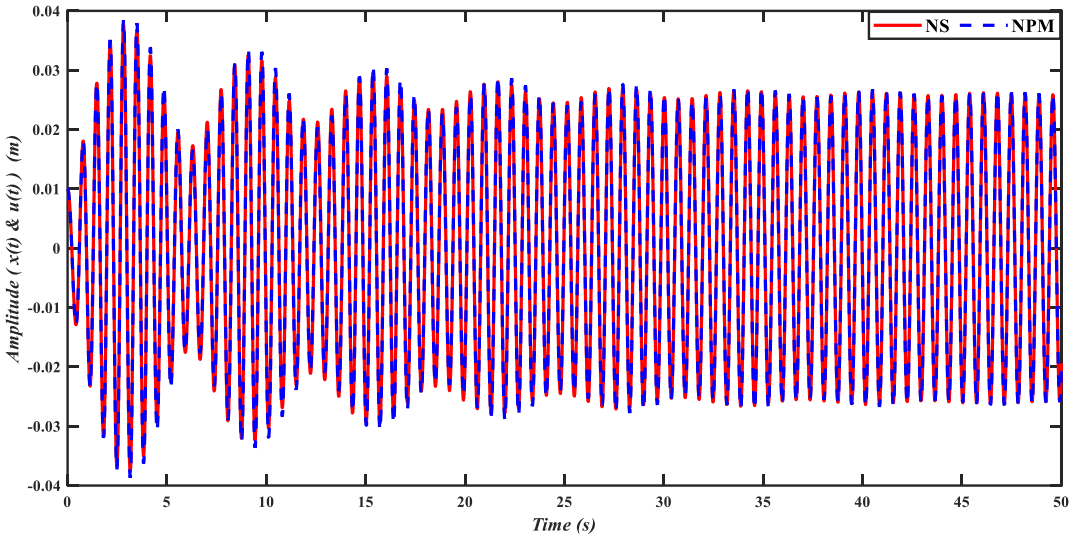

Figure 3. Demonstrates a comparison between the NS for $x(t)$ and NPM for $u(t)$.

3.2. Stability analysis for NPM

Figure 4 illustrates the stability regions of a dynamical system in terms of the parameters A and φ^2 (y-axis), under different sets of parameters. The colored regions (red, blue, and purple) represent the unstable regions for different values of ω and α. The area below each curve represents the unstable region, while the area above the curve corresponds to the stable region for the given parameter values.

In Figure 4(a), as ω increases, the unstable region expands, and the stability boundary shifts upward, indicating that the system becomes less stable with increasing ω. Thus, a higher critical value of φ^2 is required to achieve stability at higher frequencies.

In contrast, Figure 4(b) shows that as α decreases, the unstable region shrinks, and the boundary curve moves downward. This implies that the system becomes more stable at lower α values. A smaller α allows the system to remain stable over a wider range of both φ^2 and A.

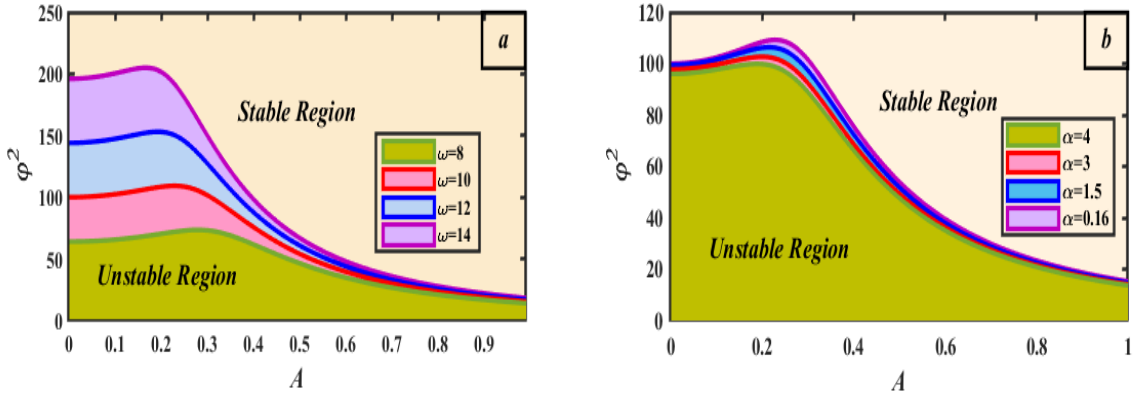

Figure 4. Shows the stable and unstable regions at different values of ω and α.

3.3. Illustrates the time history and the polar plot at different parameters

To display the influences of each parameter α, f, δ_1, and β_1 in the amplitude $u(t)$ of the wave solution of Eq (19) are observed throughout the time history Figures (5)–(8). Figure 5 highlights the significance of the damping coefficient α. The solution amplitude decreases as the damping coefficient increases. Therefore, it can be concluded that this parameter contributes to stabilizing the system's response. Additionally, the influence of the external (stimulated) force f is also depicted in Figure 6. As shown, the solution amplitude increases with the growth of the excitation force, suggesting that this parameter weakens the stability profile. Also, the effect of the nonlinearity parameter δ_1 is illustrated in Figure 7. It is generally recognized that an increase in this factor leads to a decrease in the solution's amplitude. Hence, one could argue that this parameter contributes positively to system stability.

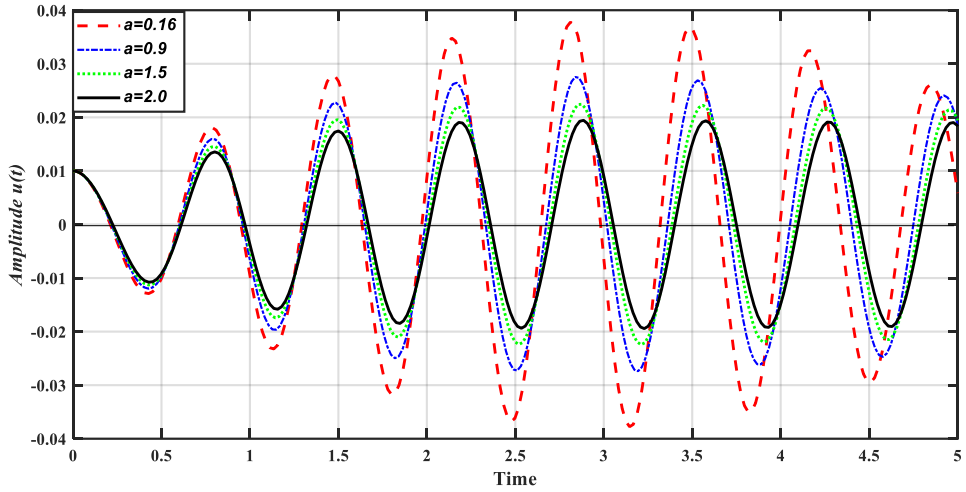

Figure 5. Illustrates the effect of α.

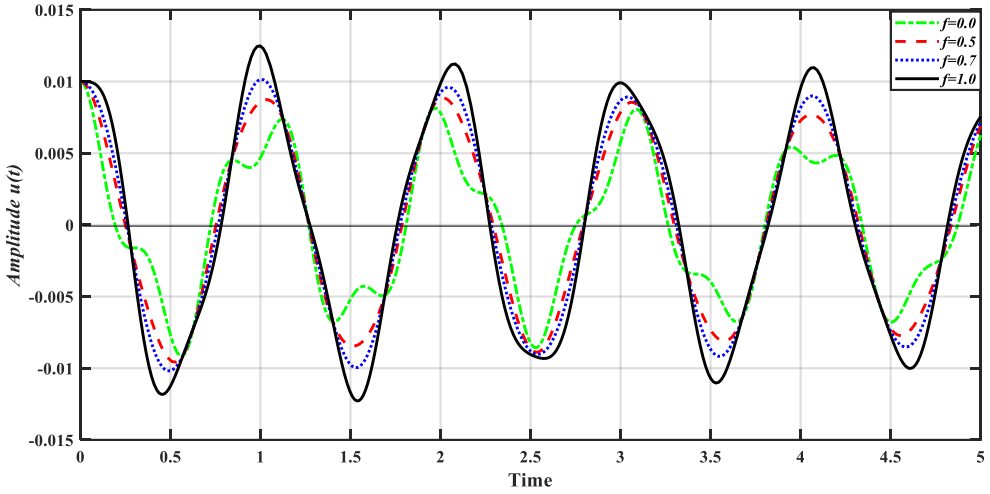

Figure 6. Illustrates the effect of f.

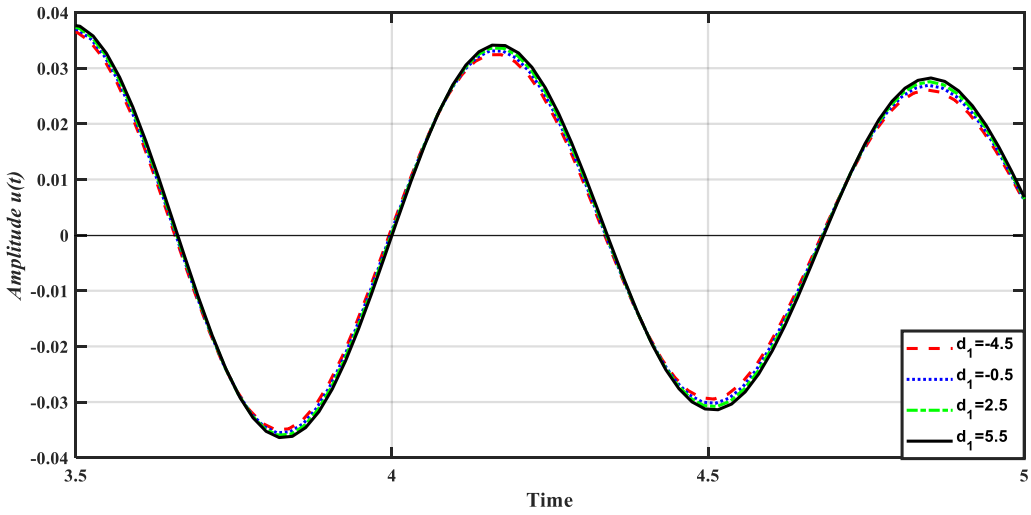

Figure 7. Illustrates the effect of δ_1.

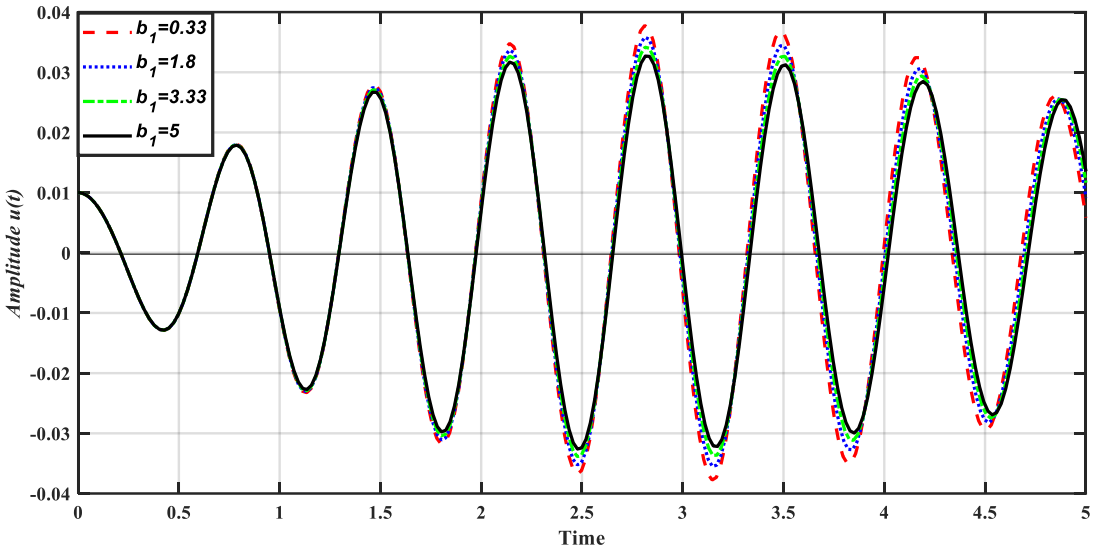

Figure 8. Illustrates the effect of β_1.

Finally, Figure 8 further demonstrates the role of the nonlinear coefficient β_1. From this figure, an increase in nonlinearity results in a reduced amplitude. Thus, it can be concluded once more that this nonlinear coefficient enhances the stability of the system.

A polar plot of the solution of Eq (19) is created at the given values of the parameters $A = 0.01, 0.015, 0.03$ and $\Omega = 7, 10, 12$, as indicated in Figures 9 and 10, respectively. These figures show how well the related solution performs when a slight alteration to its starting state and the excitation frequency is considered. Rotational symmetry is commonly observed in plots with a floral shape. This indicates that after a given angle, the plot appears the same when rotated around the center. Each of the "branches" or petals is the same size and form, and they are all evenly spaced. To put it briefly, the plot's symmetrical structure, radial pattern, and relationship to polar coordinates will be highlighted. The petals, on the other hand, stand for periodic or oscillating behavior in the radial direction. The

number of times a particular mathematical function repeats itself in the polar equation, for instance, may be connected to the number of petals, as shown in Figure 9. It is discovered that the size of the petals decreases as the values of A increases. Now for the excitation frequency Ω we can see that for small Ω it gives a simple floral shape without any repetition of petals as shown in Figure 10(a). With the rise in the quantities of Ω, the rotation of the petals in the floral shape increased regularly around the center of the shape as illustrated in Figure 10(b), but as the value of Ω exceeds number 10, we found that the floral shape was irregular as presented in Figure 10(c).

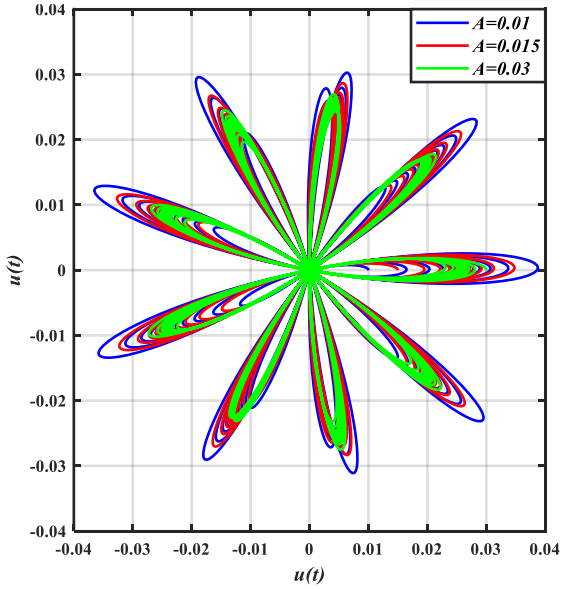

Figure 9. The system's polar graphs at $A = 0.01$, $A = 0.015$ and $A = 0.03$.

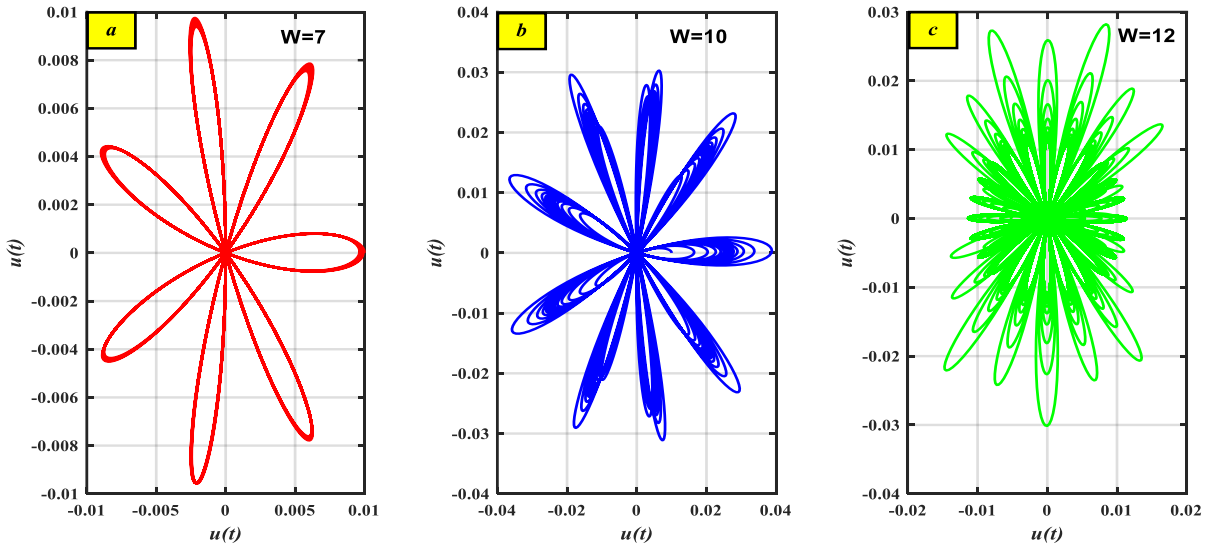

Figure 10. The system's polar graphs with (a) $\Omega = 7$, (b) $\Omega = 10$, and (c) $\Omega = 12$.

Throughout the period $[0,50\pi]$, Figures 11 and 12 have been displayed to reflect the function $u(t)$in a polar shape by the several options of $f = 0.2, 0.5, 0.9$ and $\alpha = 0.16, 0.8, 1.5$ separately. The representation of this simulation gives the structure of the floral shape with branches without any fill for the smallest value of f in Figure 11(a). On the contrary, the branches are filled with repeated petals as the values of f increased, as appeared in Figures 11(b) and 11(c). Figures (12a)–(12c) showed that there are no differences in changing the values of α , and we get the same plots.

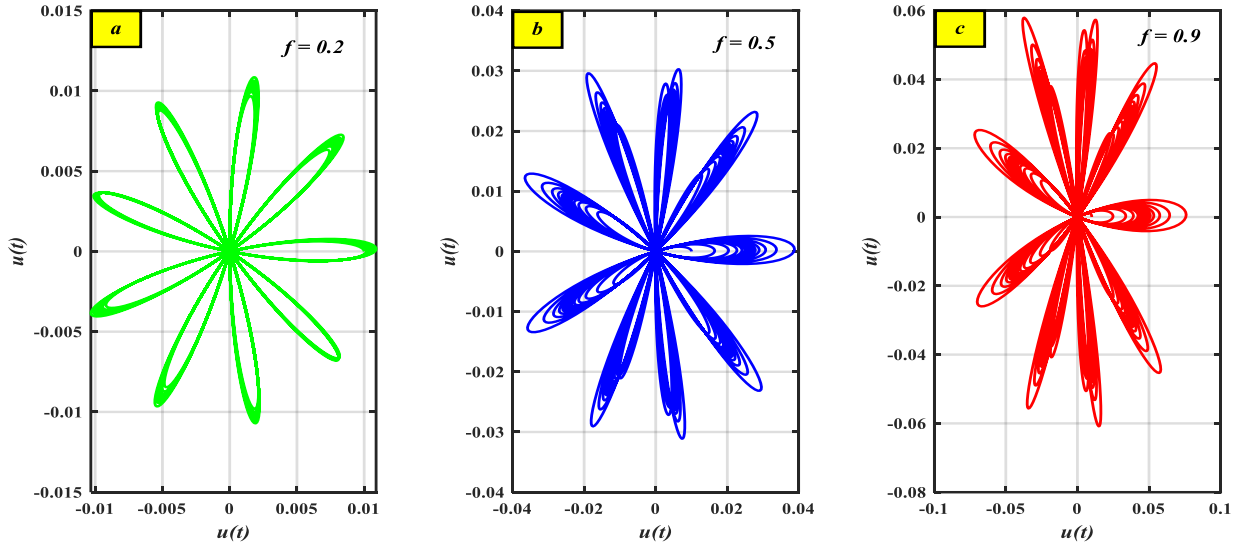

Figure 11. The system's polar graphs with (a) $f = 0.2$, (b) $f = 0.5$, and (c) $f = 0.9$.

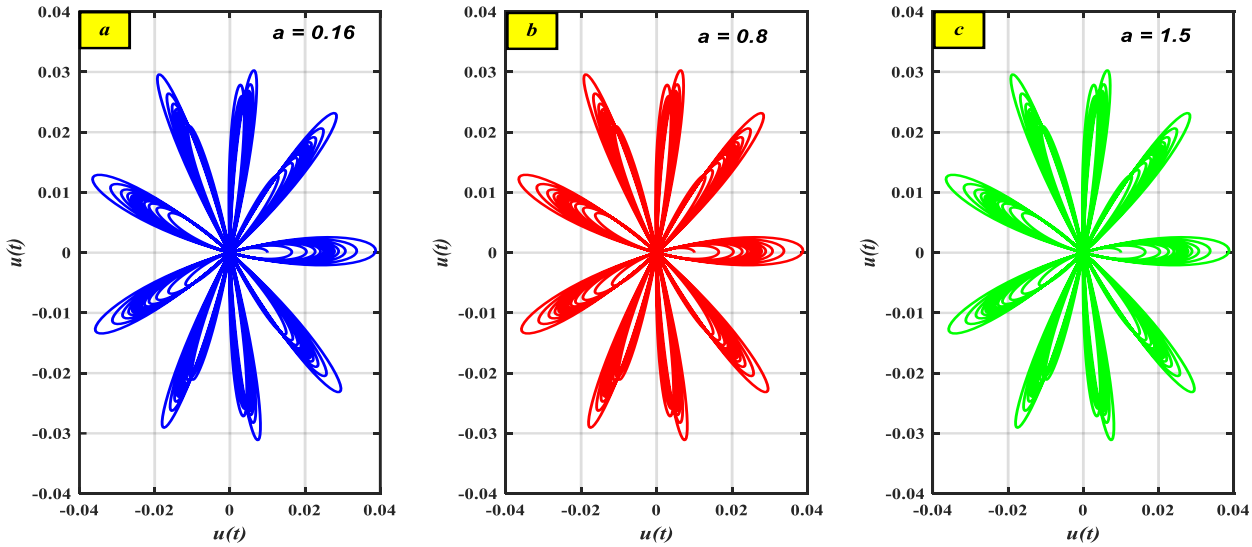

Figure 12. The system's polar graphs with (a) $\alpha = 0.16$, (b) $\alpha = 0.8$, and (c) $\alpha = 1.5$.

4. The framework's technique with NDF control

4.1. Equations of motion under control with a primary case ($\Omega = \omega + \sigma$)

The dynamical algorithm's equations of motion are outlined below [43]. The mathematical framework uses the negative feedback of the appropriate velocity concluded result as a control force after it has been integrated with NDF control.

$$\left.\begin{aligned}\ddot{x} + \varepsilon\alpha\dot{x} + \varepsilon\beta_1\dot{x}^3 + \varepsilon\beta_2\dot{x}^5 + \omega^2 x + \varepsilon\gamma_1 x^3 + \varepsilon\gamma_2 x^5 + \varepsilon\delta_1(x\dot{x}^2 + x^2\ddot{x}) + \varepsilon\delta_2(x^3\dot{x}^2 + x^4\ddot{x})\\ = \varepsilon f\cos\Omega t + \varepsilon G_1\dot{v}\end{aligned}\right\} \quad (23)$$

$$\ddot{v} + \omega_1^2 v + 2\varepsilon\mu_1\dot{v} = -\varepsilon G_2\dot{x}. \quad (24)$$

Here x is the cantilever beam's dimensionless placement. ω is the natural frequency of the framework. Ω is the frequency of excitation. αdenotes the damping coefficient. β_i, γ_i, and $\delta_i (i = 1,2)$ are factors for nonlinearity terms. f is the system's dimensionless excitation force.

v is the NDF's transverse displacements that are linked to x. The control's natural frequencies are expressed with ω_1. Additionally, the damping coefficients of the control are referred to using μ_1. G_1 is the constant gain for the control signals, and G_2 is the feedback signal gain.

For a better understanding of the structure's dynamical historical records (23) and (24), both with and without the NDF controller, we examine one of the most critical resonance cases—simultaneous primary and 1:1 internal resonance ($\omega_1 \approx \omega, \Omega \approx \omega$). RK-4 has been employed to mathematically calculate the dynamical algorithm's reproduction that was previously discussed, with the underlying assumptions $x(0) = 0.01; \dot{x}(0) = 0; v(0) = 0; \dot{v}(0) = 0$.

The MATLAB® software controller serves as the foundation for these computations obtained. Thus, the parameters used for the model are:

$$\omega = 10; \alpha = 0.16; \beta_1 = 0.3331; \beta_2 = 0.1299; \gamma_1 = 22.5; \gamma_2 = 0.1319;$$

$$\delta_1 = -4.5; \delta_2 = 2.2; f = 0.5; \Omega = 10; \omega_1 = 10.$$

Figure 13a displays the time history for the dynamical framework's steady-state amplitude in the absence of the controller. The amplitude increases to 0.0970763 for x, as can be shown. The phase plane of x is immediately described in Fig. 11b. On the other side, Figure 14(a) displays the reflected construction's amplitude after the NDF controller's merger. Figure 14(c) exhibits this. It concludes that the amplitudes expand 2.71618×10^{-6} for x with modest amplitude values for NDF. Thus, when talking about this control, the 100% for x ratios show the reduced vibration amplitudes. Finally, the effectiveness of the NDF control which is represented by E_a(E_a =the construction's steady-state amplitude before NDF divided by thereafter controlling) 35740 for x .

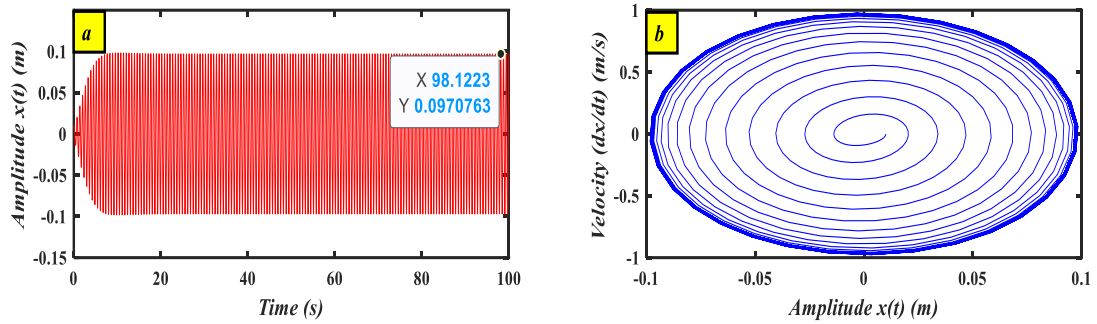

Figure 13. The dynamic framework with no controller.

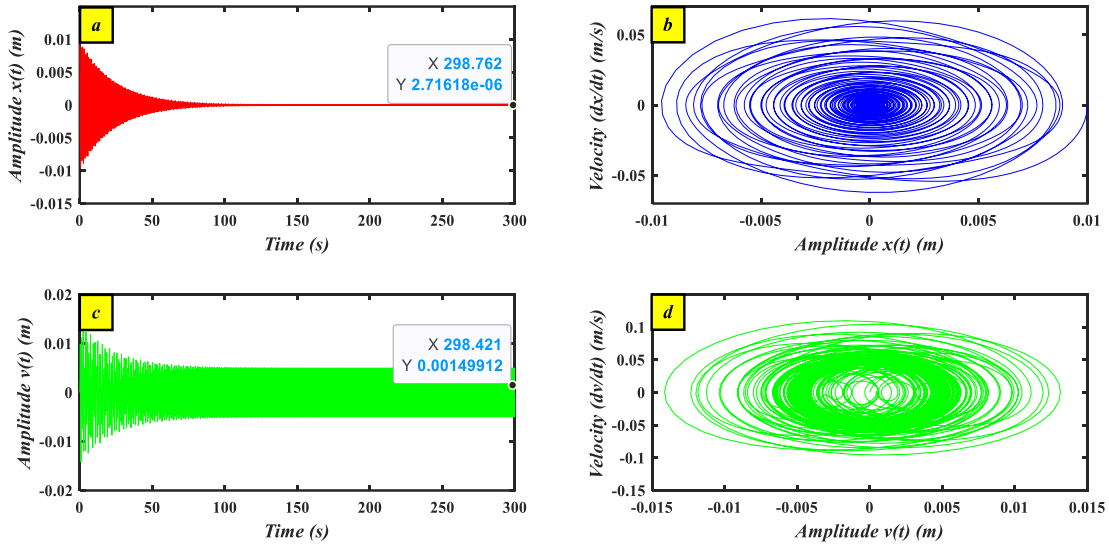

Figure 14. (a-b) The dynamic framework's amplitudes applying the control system using NDF; (c-d) the NDF's amplitudes control system

4.2. Analysis of perturbations (MTSM)

The MTSM can be used to derive the approximate solution of Eqs (23) and (24) [3, 44]. By looking for the solution in the form, we obtained first-order approximation solutions for Eqs (23) and (24).

$$x(T_0, T_1, \varepsilon) = \sum_{n=0}^{1} \varepsilon^n x_n(T_0, T_1) + O(\varepsilon^2), \tag{25}$$

$$v(T_0, T_1, \varepsilon) = \sum_{n=0}^{1} \varepsilon^n v_n(T_0, T_1) + O(\varepsilon^2), \tag{26}$$

where the fast and slow time scales are denoted by T_0 and T_1, respectively, and ε is a tiny perturbation parameter. The derivatives of time are converted into

$$\frac{d}{dt} = D_0 + \varepsilon D_1, \tag{27}$$

$$\frac{d^2}{dt^2} = D_0^2 + 2\varepsilon D_0 D_1, \tag{28}$$

$$T_n = \varepsilon^n t, D_n = \partial/\partial T_n, (n = 0,1). \tag{29}$$

By replacing equations, we were able to get the following set of ODEs (25)–(29) into Eqs (24)–(26) and calculating the coefficients of the identical power of ε concerning both opposing viewpoints:

$$O(\varepsilon^0): (D_0^2 + \omega^2)x_0 = 0, \tag{30}$$

$$(D_0^2 + \omega_1^2)v_0 = 0, \tag{31}$$

$$O(\varepsilon^1):$$

$$\left.\begin{aligned}&(D_0^2 + \omega^2)x_1 = -2D_1\left(i\omega A e^{i\omega T_0}\right) - \alpha\left(i\omega A e^{i\omega T_0}\right) - \beta_1\left(-i\omega^3 A^3 e^{3i\omega T_0} + 3i\omega^3 A^2 \bar{A} e^{i\omega T_0}\right)\\&-\beta_2\left(i\omega^5 A^5 e^{5i\omega T_0} - 5i\omega^5 A^4 \bar{A} e^{3i\omega T_0} + 10i\omega^5 A^3 \bar{A}^2 e^{i\omega T_0}\right)\\&-\gamma_1\left(A^3 e^{3i\omega T_0} + 3A^2 \bar{A} e^{i\omega T_0}\right) - \gamma_2\left(A^5 e^{5i\omega T_0} + 5A^4 \bar{A} e^{3i\omega T_0} + 10A^3 \bar{A}^2 e^{i\omega T_0}\right)\\&-\delta_1\left(-2A^3\omega^2 e^{3i\omega T_0} - 2A^2 \bar{A}\omega^2 e^{i\omega T_0}\right) - \delta_2\left(-2A^5\omega^2 e^{5i\omega T_0} - 6A^4 \bar{A}\omega^2 e^{3i\omega T_0} - 8\omega^2 A^3 \bar{A}^2 e^{i\omega T_0}\right)\\&+f\cos\Omega t + G_1\left(i\omega_1 B e^{i\omega_1 T_0}\right)\end{aligned}\right\}. \tag{32}$$

$$(D_0^2 + \omega_1^2)v_1 = -[2i\omega_1 D_1 B + 2i\omega_1 B\mu_1]e^{i\omega_1 T_0} - [i\omega A G_2]e^{i\omega T_0}. \tag{33}$$

The general solutions can be obtained by eliminating the secular terms from Eqs (32) and (33), as follows

$$x_1 = \frac{1}{8\omega^2}[-i\beta_1\omega^3 A^3 - 5i\beta_2\omega^5 A^4 \bar{A} + \gamma_1 A^3 + 5\gamma_2 A^4 \bar{A} - 2\delta_1 A^3\omega^2 - 6\delta_2 A^4 \bar{A}\omega^2]e^{3i\omega T_0}$$

$$+\frac{1}{24\omega^2}[i\beta_2\omega^5 A^5 + \gamma_2 A^5 - 2A^5\delta_2\omega^2]e^{5i\omega T_0}, \tag{34}$$

$$v_1 = 0, \tag{35}$$

where complex functions A and B are in T_1. We can identify the resonance case from the up solutions.

4.3. The periodic solution

By adding the detuning parameters $\sigma_i (i = 1,2)$, we may examine the system's stability at the examined resonance situation using the first-order approximation based on:

$$\Omega \approx \omega + \sigma_1, \tag{36}$$

The solvability conditions are derived by substituting the secular and small-divisor terms from the first approximations in Eqs (32) and (33) into Eq (36)

$$D_1 A = \frac{-A\alpha}{2} - \frac{3\beta_1\omega^2 A^2 \bar{A}}{2} - 5\beta_2\omega^4 A^3 \bar{A}^2 + \frac{3i\gamma_1 A^2 \bar{A}}{2\omega} + \frac{5i\gamma_2 A^3 \bar{A}^2}{\omega}$$

$$-i\delta_1 A^2 \bar{A}\omega - 4i\delta_2\omega A^3 \bar{A}^2 - \left(\frac{if}{4\omega}\right)e^{i\sigma_1 T_0} + \frac{\omega_1 G_1 B}{2\omega}e^{i\sigma_2 T_0}, \tag{37}$$

$$D_1 B = -B\mu_1 - \frac{\omega A G_2}{2\omega_1} e^{-i\sigma_2 T_0}. \tag{38}$$

Equations (37) through (38) can be solved using the polar form as

$$A = \frac{1}{2} a e^{i\varphi_1}, B = \frac{1}{2} b e^{i\varphi_2}. \tag{39}$$

Here, A and B represent the amplitudes of the motion phases and the steady state, respectively. By resolving the real and imaginary components and substituting Eq (39) into Eqs (37) and (38), the following system is obtained.

$$\dot{a} = \frac{-\alpha a}{2} - \frac{3\beta_1 \omega^2 a^3}{8} - \frac{5\beta_2 \omega^4}{16} a^5 + \frac{f}{2\omega} sin\,\theta_1 + \frac{\omega_1 G_1 b}{2\omega} cos\,\theta_2, \tag{40}$$

$$a\dot{\varphi}_1 = \frac{3\gamma_1 a^3}{8\omega} + \frac{5\gamma_2 a^5}{16\omega} - \frac{\delta_1 a^3 \omega}{4} - \frac{\delta_2 \omega a^5}{4} - \frac{f}{2\omega} cos\,\theta_1 + \frac{\omega_1 G_1 b}{2\omega} sin\,\theta_2, \tag{41}$$

$$\dot{b} = -b\mu_1 - \frac{\omega a G_2}{2\omega_1} cos\,\theta_2, \tag{42}$$

$$b\dot{\varphi}_2 = \frac{\omega a G_2}{2\omega_1} sin\,\theta_2, \tag{43}$$

Where,

$$\theta_1 = \sigma_1 T_1 - \varphi_1, \quad \theta_2 = \sigma_2 T_1 - \varphi_1 + \varphi_2. \tag{44}$$

4.4. The equations for the frequency response (FRE)

At $\dot{a} = \dot{b} = \dot{\theta}_1 = \dot{\theta}_2 = 0$, the cantilever beam model with NDF controllers' steady-state analysis is completed, matching the fixed point of Eqs (40)–(44). The frequency response equations for the effective case ($a \neq 0$ and $b \neq 0$) can therefore be obtained as follows:

$$0 = \frac{-\alpha a}{2} - \frac{3\beta_1 \omega^2 a^3}{8} - \frac{5\beta_2 \omega^4}{16} a^5 + \frac{f}{2\omega} sin\,\theta_1 + \frac{\omega_1 G_1 b}{2\omega} cos\,\theta_2, \tag{45}$$

$$a\sigma_1 = \frac{3\gamma_1 a^3}{8\omega} + \frac{5\gamma_2 a^5}{16\omega} - \frac{\delta_1 a^3 \omega}{4} - \frac{\delta_2 \omega a^5}{4} - \frac{f}{2\omega} cos\,\theta_1 + \frac{\omega_1 G_1 b}{2\omega} sin\,\theta_2, \tag{46}$$

$$0 = -b\mu_1 - \frac{\omega a G_2}{2\omega_1} cos\,\theta_2, \tag{47}$$

$$b(-\sigma_2 + \sigma_1) = \frac{\omega a G_2}{2\omega_1} sin\,\theta_2. \tag{48}$$

Equations (45) and (46) are squared and added, and we obtain

$$\left.\begin{aligned}\left(\frac{f}{2\omega}\right)^2 &= \left(\frac{\alpha a}{2}+\frac{3\beta_1\omega^2a^3}{8}+\frac{5\beta_2\omega^4}{16}a^5-\frac{\omega_1G_1b}{2\omega}cos\,\theta_2\right)^2\\ &+\left(-a\sigma_1+\frac{3\gamma_1a^3}{8\omega}+\frac{5\gamma_2a^5}{16\omega}-\frac{\delta_1a^3\omega}{4}-\frac{\delta_2\omega a^5}{4}+\frac{\omega_1G_1b}{2\omega}sin\,\theta_2\right)^2\end{aligned}\right\}. \tag{49}$$

Additionally, the values of trigonometric functions are obtained from Eqs (45)–(48) as follows:

$$sin\,\theta_1=\frac{2\omega}{f}\left[\frac{\alpha a}{2}+\frac{3\beta_1\omega^2a^3}{8}+\frac{5\beta_2\omega^4}{16}a^5+\frac{\omega_1^2\mu_1G_1b^2}{\omega^2aG_2}\right], \tag{50}$$

$$cos\,\theta_1=\frac{2\omega}{f}\left[-a\sigma_1+\frac{3\gamma_1a^3}{8\omega}+\frac{5\gamma_2a^5}{16\omega}-\frac{\delta_1a^3\omega}{4}-\frac{\delta_2\omega a^5}{4}+\frac{\omega_1^2G_1b^2(-\sigma_2+\sigma_1)}{\omega^2aG_2}\right], \tag{51}$$

$$sin\,\theta_2=\frac{2\omega_1b(-\sigma_2+\sigma_1)}{\omega aG_2}, \tag{52}$$

$$cos\,\theta_2=\frac{2\omega_1(-b\mu_1)}{\omega aG_2}. \tag{53}$$

After squaring and adding the results of substituting Eqs (52) and (53), we have

$$[b\mu_1]^2+[b(-\sigma_2+\sigma_1)]^2=\left(\frac{\omega aG_2}{2\omega_1}\right)^2. \tag{54}$$

The FRE used to represent the system's steady-state solutions are given by Eqs (49) and (50).

4.5. Analysis of stability at the fixed point

Let us start using the following procedure to determine the steady-state solution's stability. Let

$$a=a_{10}+a_{11},\ b=b_{10}+b_{11}\ \theta_i=\theta_{i0}+\theta_{i1},(i=1,2). \tag{55}$$

Given that a_{10}, b_{10}, and θ_{i0} meet the requirements of Eqs (45)–(48), that is regarded as a minor disturbance in relation to a_{11}, b_{11}, and θ_{i1}. Then, using (40)–(43) and just the linear terms a_{10}, b_{10}, and θ_{i0} left, we obtain

$$\begin{aligned}\dot{a}_{11}&=\left[\frac{-\alpha}{2}-\frac{9\beta_1\omega^2a_{10}^2}{8}-\frac{25\beta_2\omega^4a_{10}^4}{16}\right]a_{11}+\left[\frac{f}{2\omega}cos\,\theta_{10}\right]\theta_{11}\\&+\left[\frac{\omega_1G_1}{2\omega}cos\,\theta_{20}\right]b_{11}+\left[-\frac{\omega_1G_1b_{10}}{2\omega}sin\,\theta_{20}\right]\theta_{21},\end{aligned} \tag{56}$$

$$\begin{aligned}\dot{\theta}_{11}&=\left[\frac{\sigma_1}{a_{10}}-\frac{9\gamma_1a_{10}}{8\omega}-\frac{25\gamma_2a_{10}^3}{16\omega}+\frac{3\delta_1a_{10}\omega}{4}+\frac{5\delta_2\omega a_{10}^3}{4}\right]a_{11}\\&+\left[-\frac{f\,sin\,\theta_{10}}{2a_{10}\omega}\right]\theta_{11}+\left[-\frac{\omega_1G_1\,sin\,\theta_{20}}{2a_{10}\omega}\right]b_{11}+\left[-\frac{\omega_1G_1b_{10}}{2a_{10}\omega}cos\,\theta_{20}\right]\theta_{21},\end{aligned} \tag{57}$$

$$\dot{b}_{11} = \left[-\frac{\omega G_2}{2\omega_1} cos\,\theta_{20}\right] a_{11} + [0]\theta_{11} + [-\mu_1]b_{11} + \left[\frac{\omega a_{10} G_2}{2\omega_1} sin\,\theta_{20}\right]\theta_{21}, \tag{58}$$

$$\dot{\theta}_{21} = \left[\frac{\sigma_1}{a_{10}} - \frac{9\gamma_1 a_{10}}{8\omega} - \frac{25\gamma_2 a_{10}^3}{16\omega} + \frac{3\delta_1 a_{10}\omega}{4} + \frac{5\delta_2 \omega a_{10}^3}{4} + \frac{\omega G_2}{2b_{10}\omega_1} sin\,\theta_{20}\right] a_{11}$$

$$+\left[-\frac{f}{2a_{10}\omega} sin\,\theta_{10}\right]\theta_{11} + \left[-\frac{\omega_1 G_1}{2a_{10}\omega} sin\,\theta_{20} + \frac{(\sigma_2 - \sigma_1)}{b_{10}}\right] b_{11}$$

$$+\left[-\frac{\omega_1 G_1 b_{10}}{2a_{10}\omega} cos\,\theta_{20} + \frac{\omega a_{10} G_2}{2b_{10}\omega_1} cos\,\theta_{20}\right]\theta_{21}. \tag{59}$$

In a matrix, Eqs (59)–(62) can be expressed as follows:

$$[\dot{a}_{11} \quad \dot{\theta}_{11} \quad \dot{b}_{11} \quad \dot{\theta}_{21}]^T = [J][a_{11} \quad \theta_{11} \quad b_{11} \quad \theta_{21}]^T, \tag{60}$$

where the Jacobin matrix of Eqs (56)–(58) is denoted by $[J]$. The Jacobin matrix $[J]$ eigenvalues can be expressed as follows:

$$\lambda^4 + K_1\lambda^3 + K_2\lambda^2 + K_3\lambda + K_4 = 0. \tag{61}$$

The solutions are stable if the real component of the eigenvalue is negative; otherwise, they become unstable. Here, $K_i (i = 1,2,\ldots,4)$ represents the coefficient in Eq (61). According to the Routh-Hurwitz criterion, every root of Eq (53) must satisfy the condition that the determinant and all its principal minors are positive. Only then will Eq (61) yield negative real parts, ensuring stability.

$$D = \begin{vmatrix} K_1 & 1 & 0 & 0 \\ K_3 & K_2 & K_1 & 1 \\ 0 & K_4 & K_3 & K_2 \\ 0 & 0 & 0 & K_4 \end{vmatrix}. \tag{62}$$

5. Consequences of the modeling

5.1. Effects of the various parameters

The FRC, shown in Figures (15)–(22), provide a detailed representation of the effects of various coefficients in the NDF-controlled model. Notably, the curves exhibit only stable regions, with no unstable zones. Additionally, two distinct peaks appear within the stability mode, as observed in Figure 15(a), which describes the response of the detuning parameter σ_1 against the system a, while Figure 15(b) shows the effect of σ_1 against the control b. Figure 16(a) and 16(b) illustrate how the system response curves a and the control b change against the detuning parameter σ_1 when the damping coefficient α is increased. The figure demonstrates that the cantilever beam's vibration amplitudes drop as the damping coefficient α increases on both sides with the main system and the control. Figures 17(a) and 17(b) illustrate how the structure's response curves vary when the natural frequency ω is increased. The figure indicates that the cantilever beam's vibration amplitudes fall as the natural frequency ω increases on the opposite sides for both the system a and the control b. Figures 18(a) and 19(b) depict the influence of the external force f on the system response curves. By

viewing this picture, as the external excitation force f increases, the amplitude of a becomes higher in each side with the same stable region varying for both systems a and the control b.

According to Figures 19(a) and 19(b) , the system's amplitude a and the control b increase as the gain G_1 values rise on both opposing sides. In the same way, Figures 20(a) and 20(b) demonstrate the impact of the damper gain G_2 on the amplitude of the system a and the control b , which indicates that the amplitude increases with the values of G_2.

Figures 21(a) and 21(b) highlight the operation of the damping coefficients of the control μ_1 which shows that, while the damping coefficients of the control μ_1 increases or decreases, the amplitude of the system and the control keep at the same value without any change. Finally, Figures 22(a) and 22(b) give the behavior of the system in the case of changing the values of the detuning parameter σ_2, which indicates that the amplitude of a and the control b neither increases nor decreases as the value of σ_2 is changed.

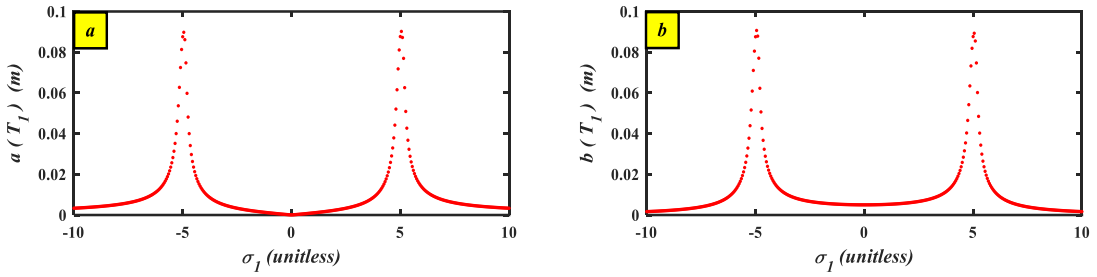

Figure 15. After the control is added, the frequency response path of the nonlinear vibrations on the cantilever beam is obtained (a) Illustrate the response of σ_1 via the system a. (b) Illustrate the response of $\sigma_1$via the control b.

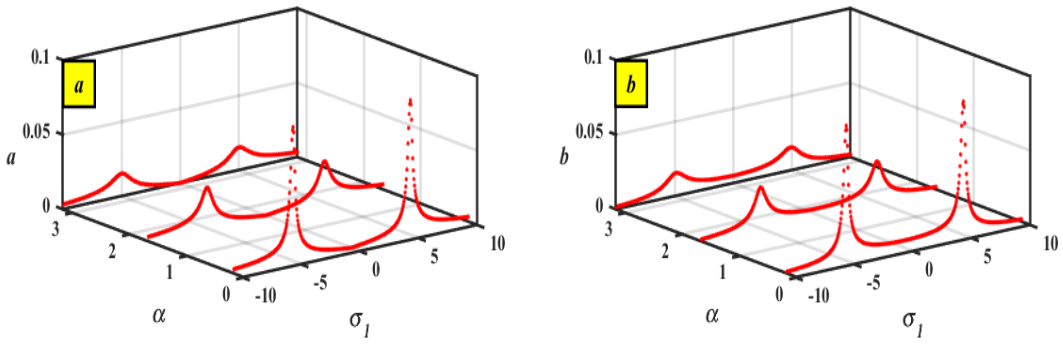

Figure 16. After the control is added, the frequency response path of the nonlinear vibrations on the cantilever beam are obtained at various values of α. (a) Illustrate the response of σ_1 via the system a. (b) Illustrate the response of $\sigma_1$via the control b.

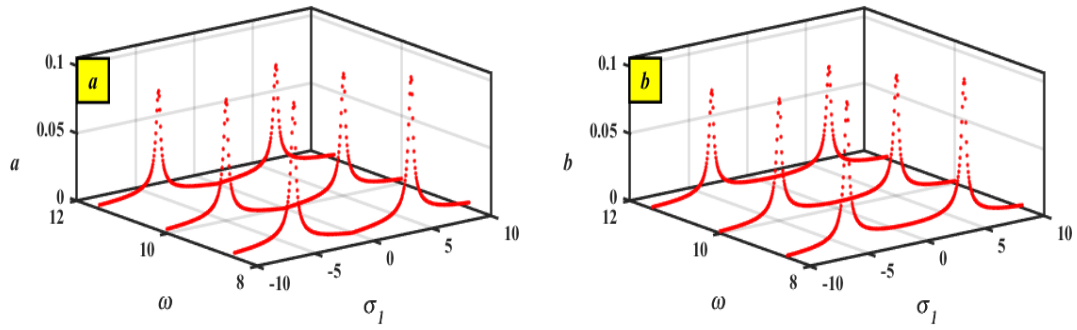

Figure 17. After the control is added, the frequency response path of the nonlinear vibrations on the cantilever beam are obtained at various values of ω. (a) Illustrate the response of σ_1 via the system a. (b) Illustrate the response of $\sigma_1$via the control b.

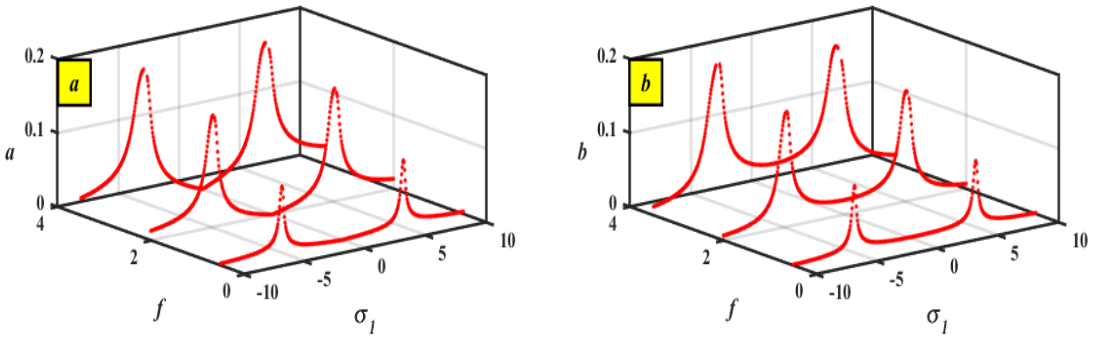

Figure 18. After the control is added, the frequency response path of the nonlinear vibrations on the cantilever beam are obtained at various values of f. (a) Illustrate the response of σ_1 via the system a. (b) Illustrate the response of $\sigma_1$via the control b.

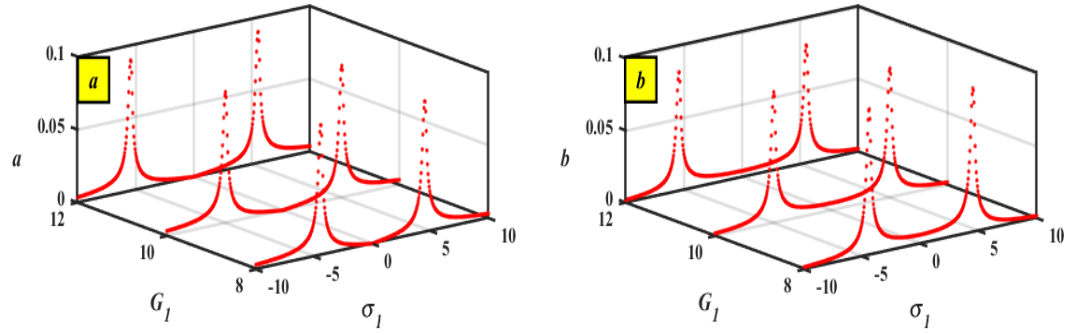

Figure 19. After the control is added, the frequency response path of the nonlinear vibrations on the cantilever beam are obtained at various values of G_1. (a) Illustrate the response of σ_1 via the system a. (b) Illustrate the response of $\sigma_1$via the control b.

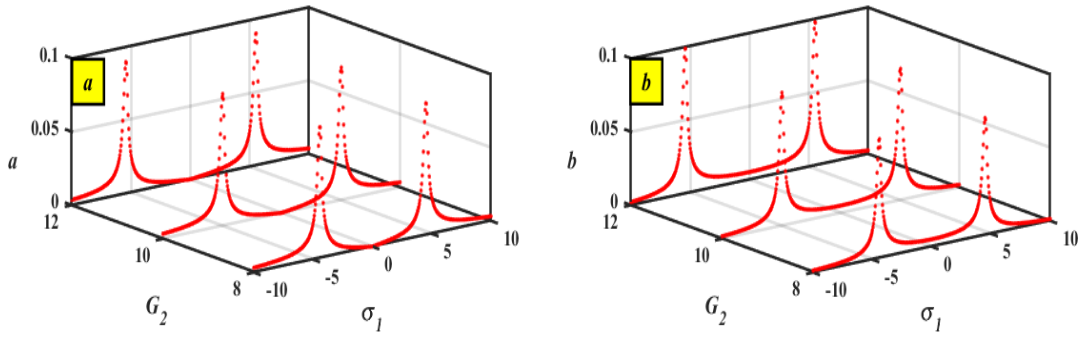

Figure 20. After the control is added, the frequency response path of the nonlinear vibrations on the cantilever beam are obtained at various values of G_2. (a) Illustrate the response of σ_1 via the system a. (b) Illustrate the response of $\sigma_1$via the control b.

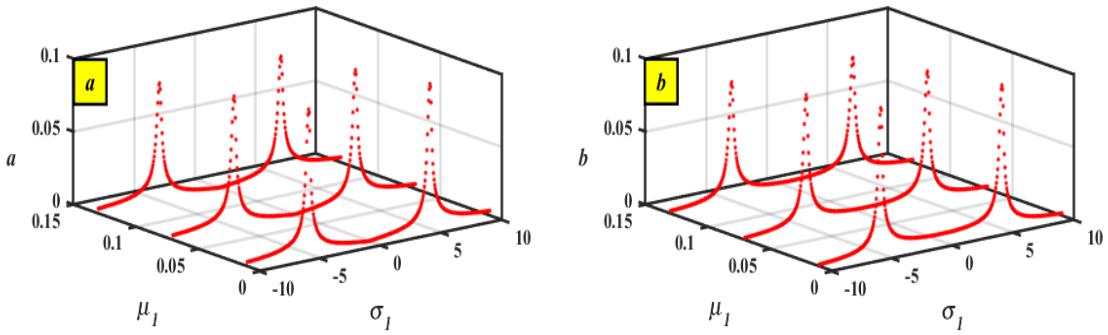

Figure 21. After the control is added, the frequency response path of the nonlinear vibrations on the cantilever beam is obtained at various values of μ_1. (a) Illustrate the response of σ_1 via the system a. (b) Illustrate the response of $\sigma_1$via the control b.

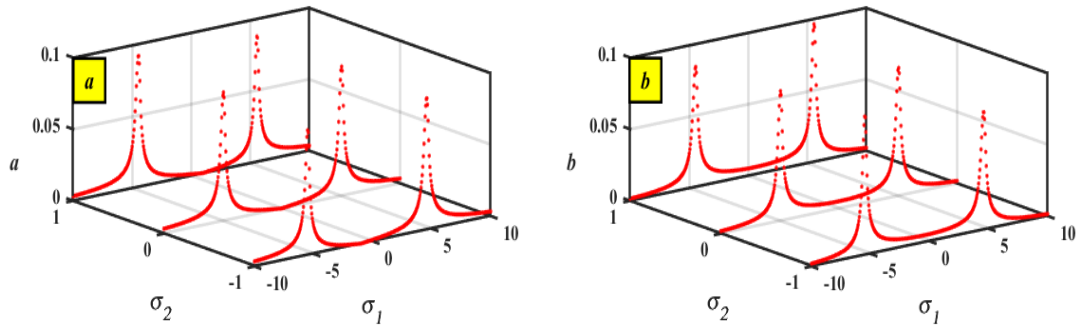

Figure 22. After the control is added, the frequency response path of the nonlinear vibrations on the cantilever beam is obtained at various values of σ_2. (a) Illustrate the response of σ_1 via the system a. (b) Illustrate the response of $\sigma_1$via the control b.

5.2. A comparison graph between the numerical modeling and the MTSM investigation

This section includes several comparison graphs to emphasize the study's objective. Figure 23 presents the frequency response curves and time-domain behavior of the uncontrolled system before and after NDF implementation, demonstrating that the NDF controller outperforms the other two in reducing vibration amplitude (PPF). Figure 24 illustrates the system's frequency response with and without NDF control, highlighting a reduction in amplitude. Additionally, Figure 25(a) and Figure 25(b) depict the analytical solutions of Eqs (40)–(43) using dashed (---) lines, which correspond to the numerical solutions of Eqs (23–24) for the main system and the controller, respectively.

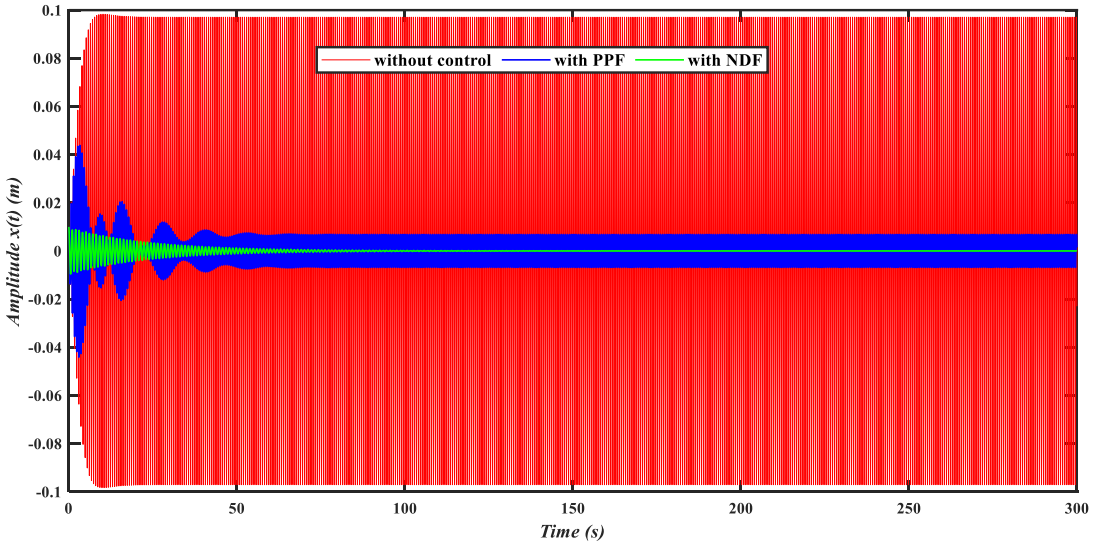

Figure 23. Time histories (waveforms) for x without control, with PPF control, and with NDF control is compared across various controllers.

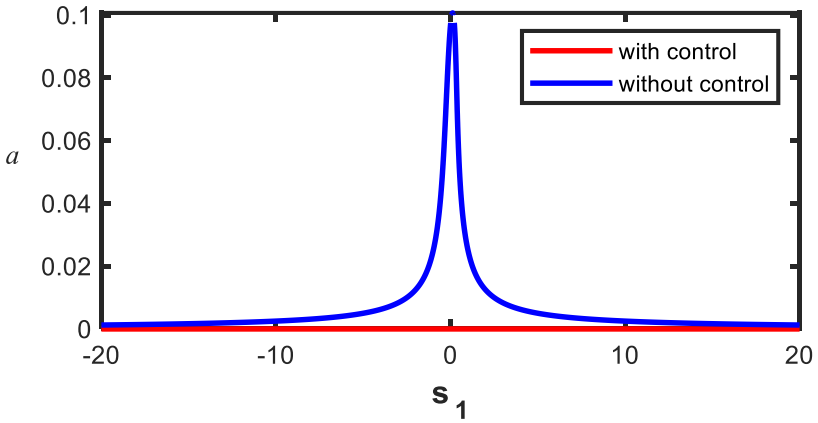

Figure 24. A comparison of the curve's frequency response before and after NDF control was added.

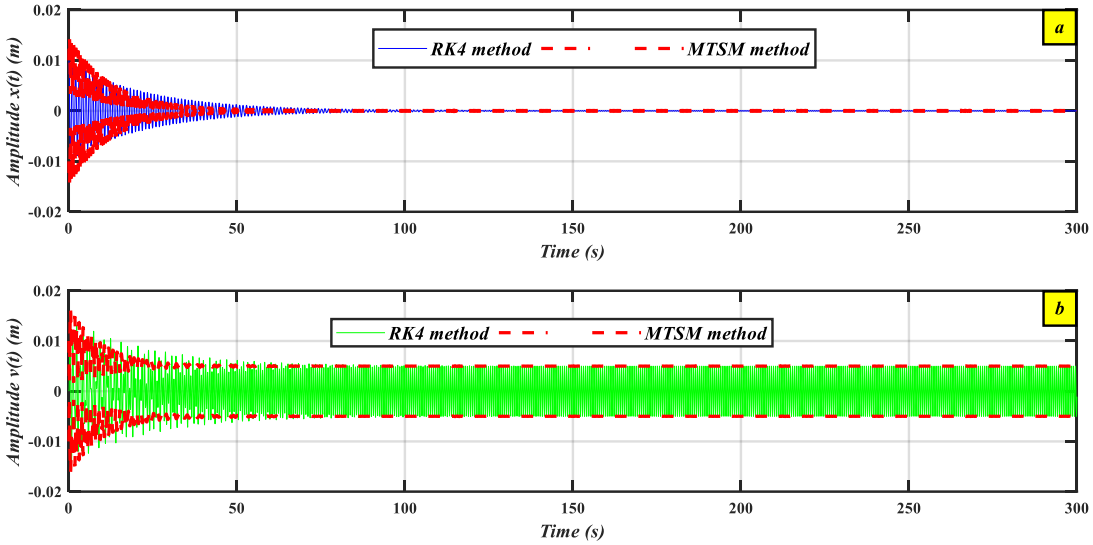

Figure 25. Comparing numerical simulation and perturbation analysis for the basic system using the NDF approach for the main system in (a) and the controller in (b).

6. Characterization of bifurcation

Looking into unpredictable actions is essential for comprehending the intricacy of structures with nonlinear dynamics in this portion of the article. The system undergoes transitions whenever its parameters change, as observed in our case. A wide range of conduct, from predictable cyclical movement to chaos, might result from these alterations. Bifurcation visualization summarizes these transitions effectively, illustrating the mechanism's evolution as a crucial factor that varies. MATLAB has been utilized to evaluate the altered mechanism, and the Poincaré maps, phase portraits, and bifurcation charts are also presented in the following results. The indeterminate variant of Eqs (18) and (19) was used to conduct the bifurcation investigation, where the second-order phase differential equations were converted into a primary scheme that was identical. The bifurcation diagrams in Figures (26)–(34) highlight the critical points at which the operation of the entire framework changes, often transitioning from chaotic or complex dynamics to quasiperiodic behavior. These variations show the places of bifurcation, which are crucial for determining stability transitions within the system. Quasiperiodic motion frequently develops as Ω (the bifurcation parameter) falls, ultimately resulting in chaotic motion. In many nonlinear systems, this transition is typical for the behavior to go from quasiperiodic to chaotic.

Simulated two different gain values were represented via bifurcation diagrams, G_1 and G_2. The illustrations of bifurcation for $G_1 = G_2 = 10$ shown in Figure 26 indicate the bifurcation diagram for $x$and v motion with the parameter Ω. Figure (26a) displays that the motion for x is chaotic for $1.74 \leq \Omega \leq 12.805$ and quasiperiodic for $12.805 \leq \Omega \leq 15$. Figure (26b) reveals the steps of change of $v$motion which is quasiperiodic for $0 \leq \Omega \leq 2.05$, chaotic for $2.05 \leq \Omega \leq 7.66$, and then periodic in the interval $9.64 \leq \Omega \leq 15$ (Figures (26)–(28) and Figures (31)–(34)). Blue curves show the phase portraits, while red dots show the Poincaré maps. Figure (28b) explains that at $\Omega = 4$, the red pixels start to show random deviation.

The figures produced showed numerous measurements of the damping coefficient G_1, and G_2 to show several motions of the system. Figures (27)–(29) explored when the values was $G_1 = G_2 = 10$. Figures (30)–(32) study the effect when $G_1 = G_2 = 1$. Figures (27b) and (29b) demonstrate how the red-dot pattern of the Poincaré maps is close to a single point, confirming the earlier finding that the system's periodic motion has been reflected at $\Omega = 10$ and $\Omega = 14$, respectively.

The chaotic state causes the red dots to spread and diverge randomly, as seen in Figures (28), (32), and (33), that was present in the value $\Omega = 4$ for Figures (28) and (32), and with $\Omega = 14$ for Figure (33). Also, Figure (32b) illustrates that at $\Omega = 4$, the red pixels start to show random deviation. Compared to Figure 30, which was drawn at a control value lower than the utilized control parameter, Figure 26 shows that the region of periodic motion is reduced, and the area of quasiperiodic motion is expanded.

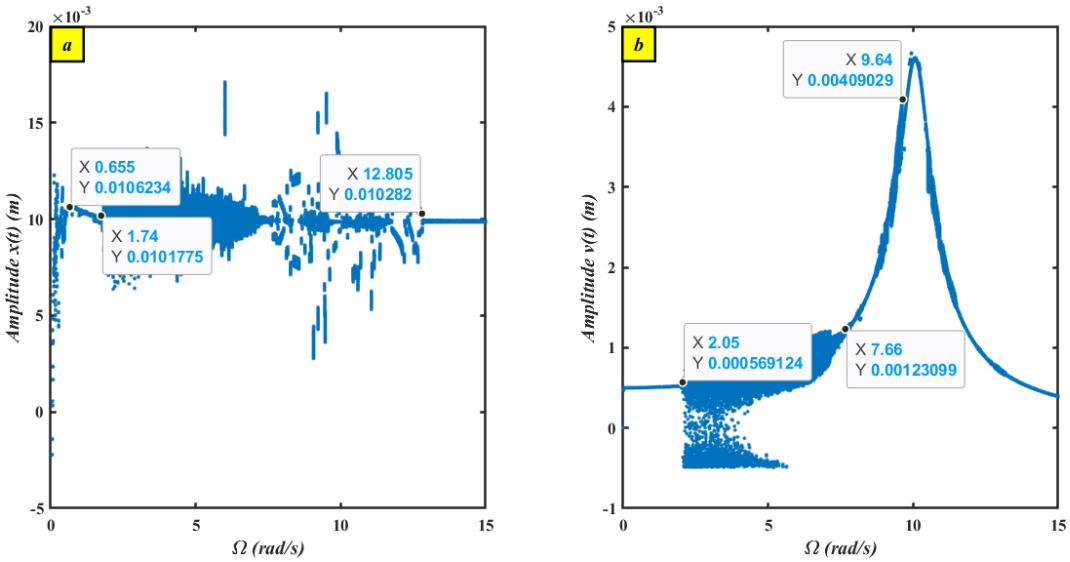

Figure 26. Bifurcation charts of x and v against Ω whenever $G_1, G_2 = 10$.

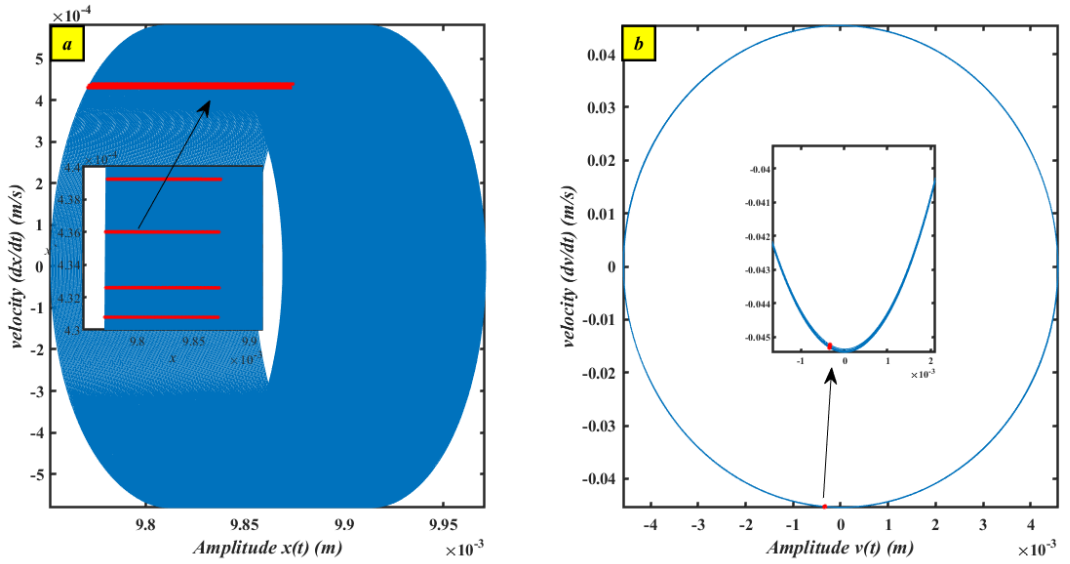

Figure 27. Emphasizes phase portraits and Poincaré diagrams for the variables are quasiperiodic for x and periodic v at $\Omega = 10$.

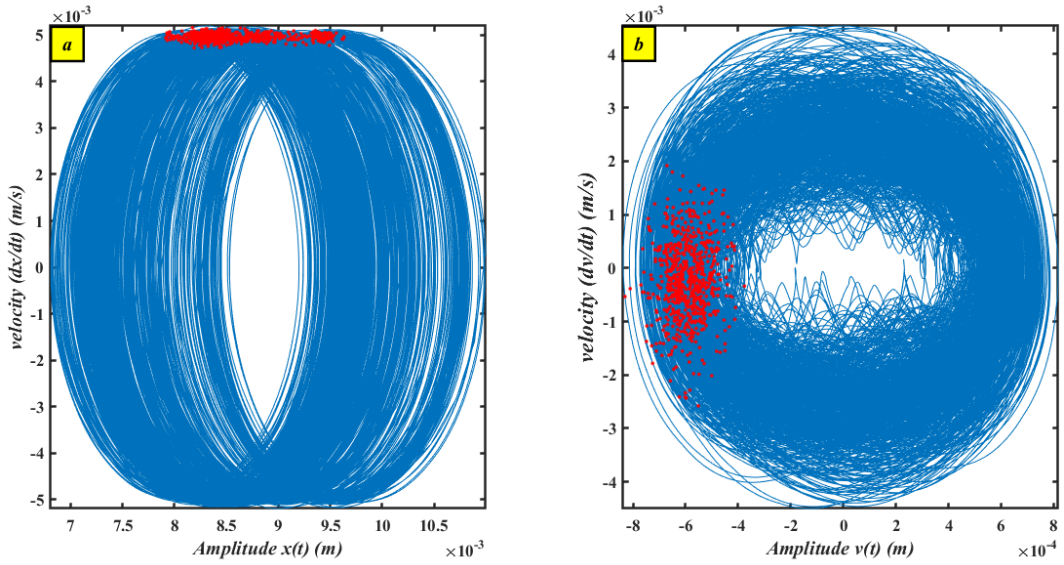

Figure 28. Emphasizes phase portraits and Poincaré diagrams for the variables, which is chaotic for x and chaotic for v at $\Omega = 4$.

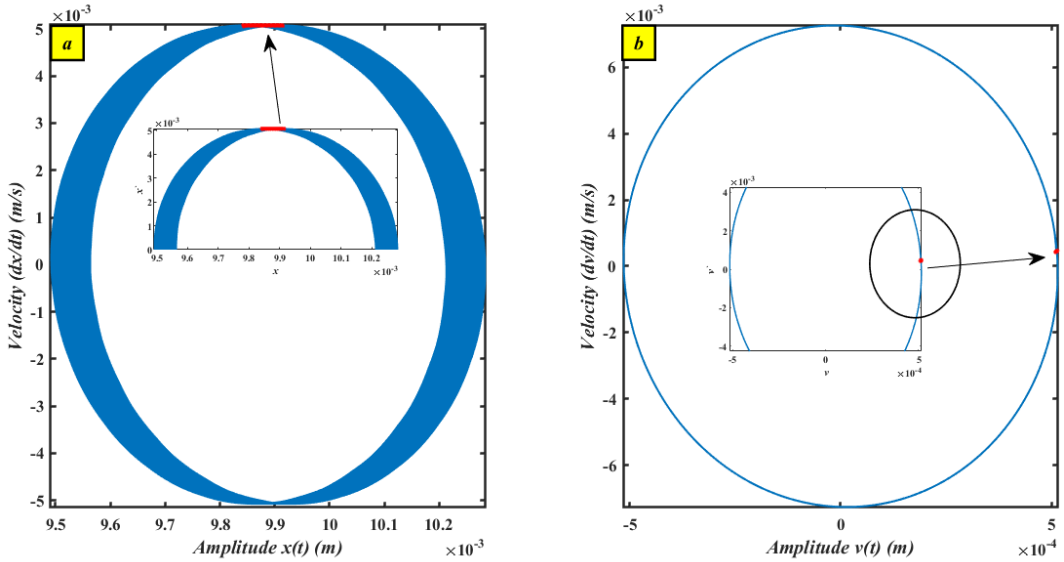

Figure 29. Emphasizes phase portraits and Poincaré diagrams for the variables, which is quasiperiodic for x and periodic for $v$at $\Omega = 14$.

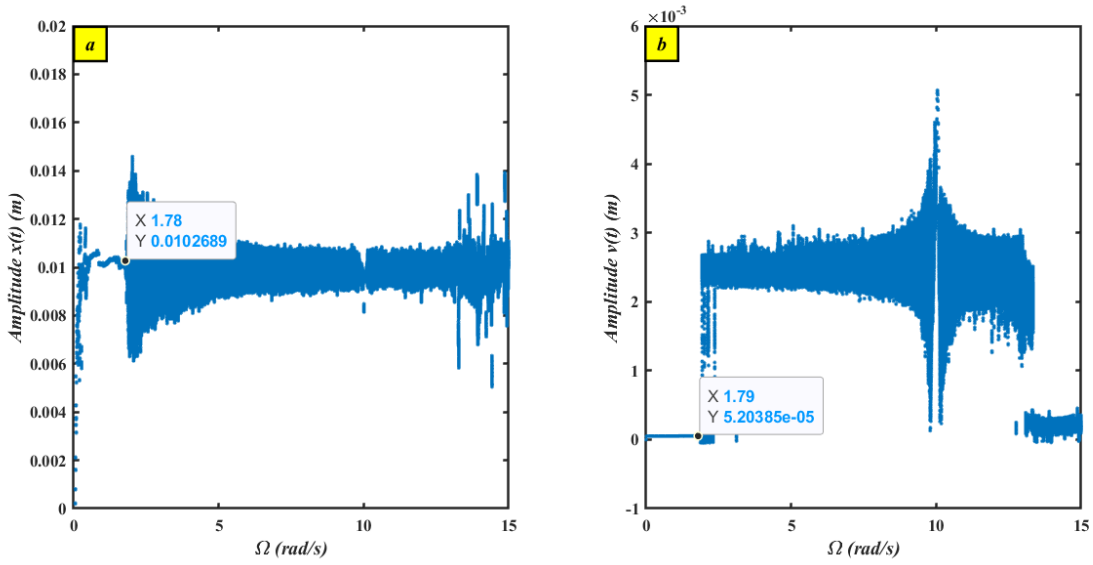

Figure 30. Bifurcation charts of x and $v$against Ω whenever $G_1, G_2 = 1$.

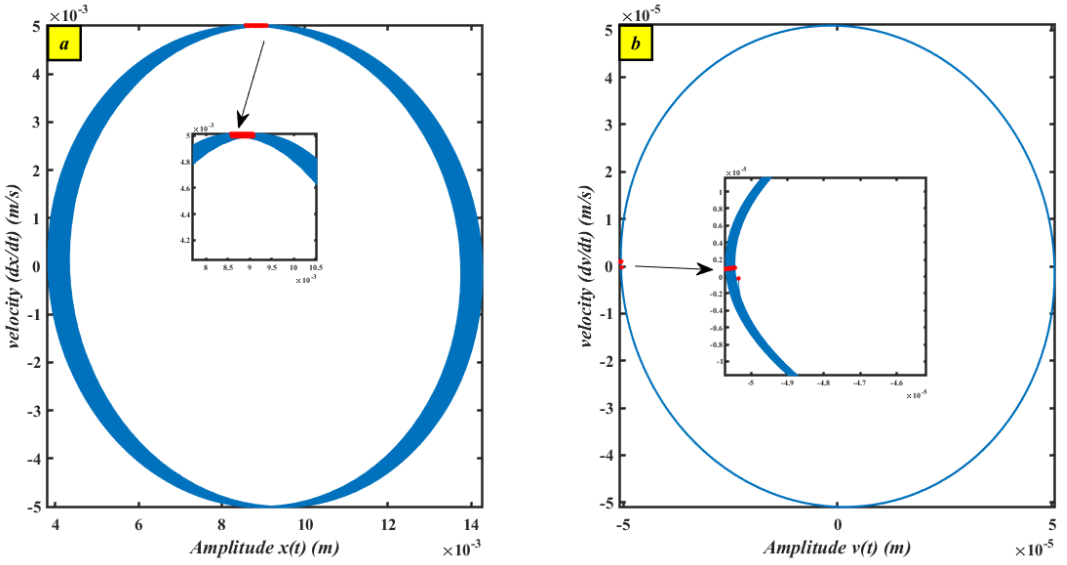

Figure 31. Emphasizes phase portraits and Poincaré diagrams for the variables, which is quasiperiodic for x and periodic for v at $\Omega = 1$.

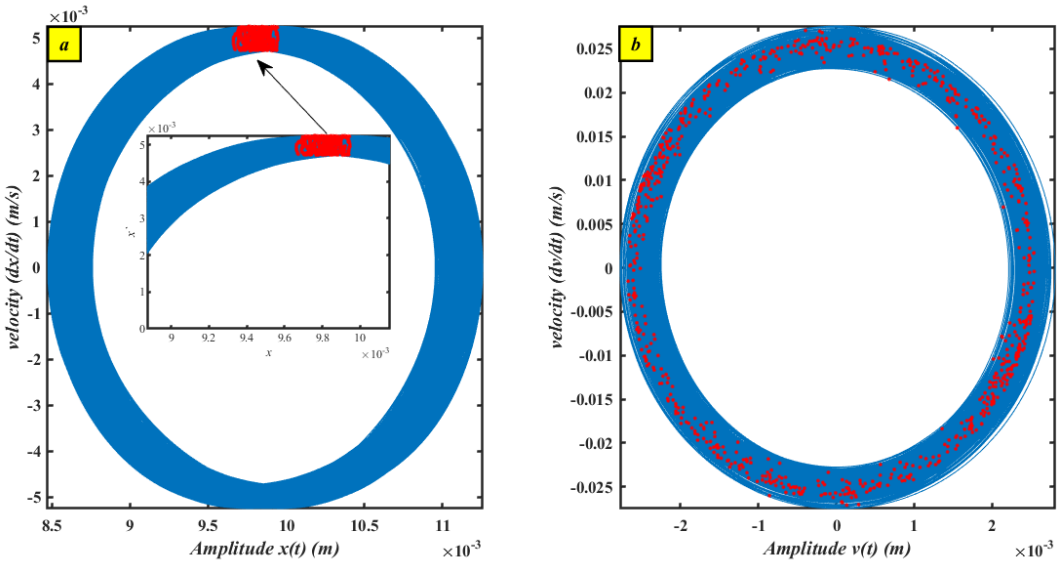

Figure 32. Emphasizes phase portraits and Poincaré diagrams for the variables, which is chaotic for x and chaotic for $v$at $\Omega = 4$.

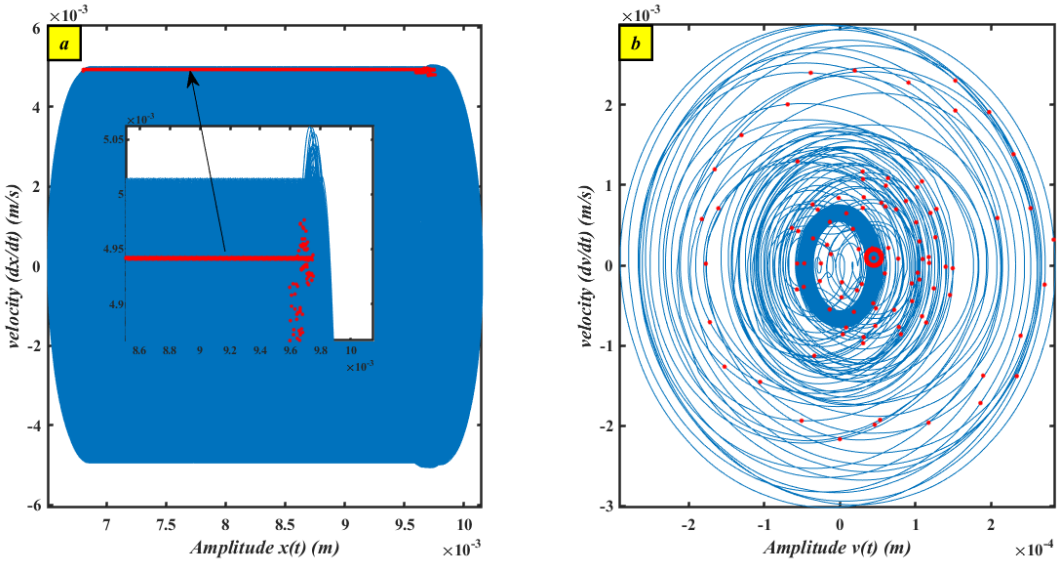

Figure 33. Emphasizes phase portraits and Poincaré diagrams for the variables, which is more chaotic for x and more chaotic for v at $\Omega = 14$.

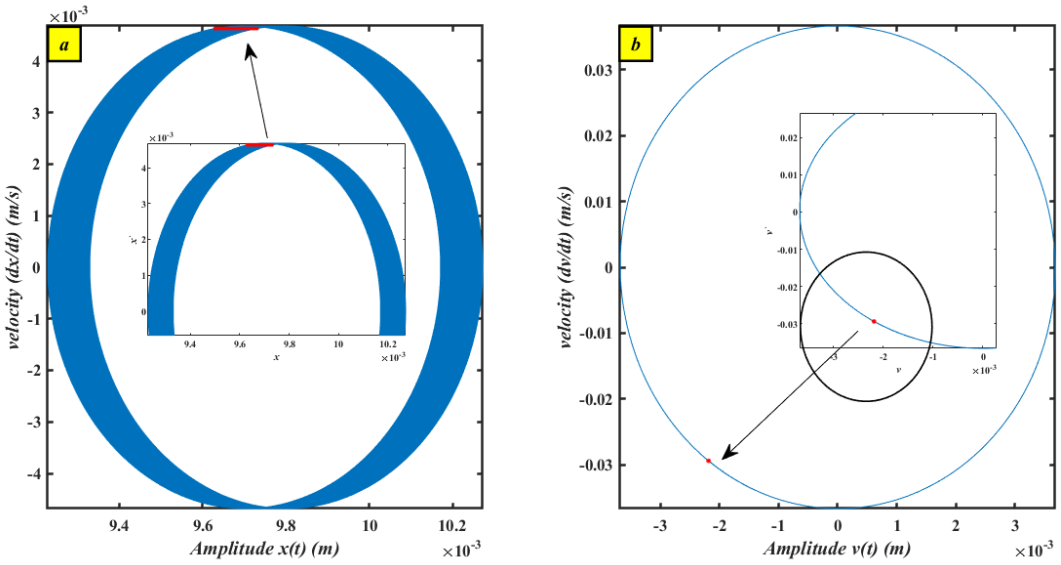

Figure 34. Emphasizes phase portraits and Poincaré diagrams for the variables, which is quasiperiodic for x and periodic for vat Ω=10.

7. Conclusions

The overall objective of this work and the key achievements can be summarized as follows.

The CBS was analyzed using the NPM, with a focus on its cyclical analytical solution. This study relies on the recently developed El-Dib [15] frequency formulation, which is comparable to He's frequency formulation in that it simplifies the nonlinear equation by transforming it into an associated linear equation with a frequency component. The linearized equation's solution closely resembles the original nonlinear problem's precise NS.

The effectiveness of the suggested strategy is demonstrated by the strong correlation between the theoretical and numerical results.

Equation (10) was also constructed using linear control, and the linear damping elements that compose the foundation were modified using NPM.

Equation (8) illustrates how this method affects the natural frequency (ω).

The investigated structure has exhibited a variety of nonlinear characteristics, including jump events, multi-solution coexistence, and sensitivity to beginning conditions, which were not present in the NPM approach. One significant feature of the linear system generated from NPM is that its parameters are simple to calculate despite containing elements of complex nonlinear factors.

Even in the presence of periodic forces, the linearization technique enables the derivation of quasi-exact solutions. The relationships between frequencies and amplitudes are easily predicted, and numerical calculations explicitly validate the accuracy and effectiveness of this novel methodology. The results align closely with precise numerical solutions, demonstrating the method's correctness. Furthermore, the approach is highly adaptable to other nonlinear configurations, making it particularly suitable for applications in manufacturing and in various scientific fields as well. Equations that are differential with one degree of freedom before controlling and two degrees of freedom following controller implementation have created the dynamic framework in this study. This framework is then subjected to NDF, a resonant control. The MTSM is quite successful in solving the controlled

simulation. The outcomes show that the NDF controller effectively lowers system vibrations, especially those that occur close to resonance.

Furthermore, it has been found that NDF can effectively eliminate the amplitude. With small amplitude values for NDF, it is concluded that the amplitudes expand for x. As a result, the 100% for $x$ratios illustrate the decreased vibration amplitudes while discussing this control. Lastly, E_a, which stands for the efficacy of the NDF control, is 35740 for x. A numerical study has been conducted to evaluate the impact of each coefficient on the redesigned controlled system within the frequency of the response curves. A comparison between the analytical and numerical analyses of the controlled framework model has also been performed. The controllable simulation was subjected to bifurcation investigation at two distinct gain levels. Three different motion types, periodic, quasi-periodic, and chaotic, are displayed and examined in the system using Lyapunov spectra, Poincaré graphs, and bifurcation plots.

8. Future work

Inertial coupling, nonlinear stiffness, nonlinear damping, and external periodic forcing—all essential for controlling spacecraft vibration and attitude—are included in our model. It is common practice to model flexible spacecraft, such as solar panels, antenna booms, or space telescopes, as rigid things with flexible appendages attached. Particularly when subjected to external excitations (such as aerodynamic drag, gravity-gradient torques, or onboard actuators), these appendages experience elastic deformation that needs to be managed or dampened. As is well-known, the rigid-body attitude control system interacts with flexible modes during maneuvers. Future work analyzing modal coupling and resonant excitation, which can be disastrous in high-precision systems (like space telescopes), will benefit greatly from this model since it leads to vibration-induced errors, energy transfer between modes, and control structure interaction (CSI). Also, there will be compensation for the time delay and to prevent adverse performance impacts [45–46].

Author contributions

Asma Alanazy: Investigation, Data curation, Writing–original draft. A. T. EL-Sayed: Conceptualization, Methodology, Software, Writing–original draft. F. T. EL-Bahrawy: Investigation, Methodology, Software and Validation, Data curation, Writing–original draft.

Use of Generative-AI tools declaration

The authors declare they have not used Artificial Intelligence (AI) tools in the creation of this article.

Acknowledgments

The authors extend their appreciation to the Deanship of Scientific Research at Northern Border University, Arar, KSA for funding this research work through the project number “NBU-FPEJ-2025-912-01”.

Conflicts of interest

The authors declare no conflicting interests.

Reference

1. R. E. Mickens, *Oscillations in planner dynamic systems*, Singapore: World Scientific, 1996. https://doi.org/10.1142/2778
2. D. Kumar, J. Singh, D. Baleanu, A hybrid computational approach for Klein-Gordon equations on Cantor sets, *Nonlinear Dyn.*, **87** (2017), 511–517. https://doi.org/10.1007/s11071-016-3057-x
3. A. H. Nayfeh, D. T. Mook. *Nonlinear oscillations*, New York: John Wiley & Sons, 1979.
4. G. M. Ismail, M. M. El-Moshneb, M. Zayed, Analytical technique for solving strongly nonlinear oscillator differential equations, *Alex. Eng. J.*, **74 (**2023**)**, 547–557. https://doi.org/10.1016/j.aej.2023.05.030
5. G. M. Ismail, M. M. El-Moshneb, M. Zayed, A modified global error minimization method for solving nonlinear Duffing-harmonic oscillators, *AIMS Math.*, **8** (2023), 484–500. https://doi.org/10.3934/math.2023023
6. G. M. Ismail, M. D. Hosen, M. Mohammadian, M. M. El-Moshneb, M. Bayat, Nonlinear vibration of electrostatically actuated microbeam, *Mathematics*, **10 (**2022**)**, 4762. https://doi.org/10.3390/math10244762
7. M. Mohammadian, G. M. Ismail, Improved harmonic balance method for analyzing asymmetric restoring force functions in nonlinear vibration of mechanical systems, *Phys. Scr.*, **99 (**2024**)**, 075280. https://doi.org/10.1088/1402-4896/ad593f
8. C. S. Liu , Y. W. Chen, A simplified Lindstedt-Poincaré method for saving computational cost to determine higher order nonlinear free vibrations, *Mathematics*, **9 (**2021**)**, 3070. https://doi.org/10.3390/math9233070
9. J. H. He, T. S. Amer, S. Elnaggar, A. A. Galal, Periodic property and instability of a rotating pendulum system, *Axioms*, **10** (2021), 191. https://doi.org/10.3390/axioms10030191
10. J. H. He, Some asymptotic methods for strongly nonlinear equations, *Int. J. Mod. Phys. B*, **20** (2006), 1141–1199. https://doi.org/10.1142/S0217979206033796
11. J. H. He, The simpler, the better: Analytical methods for nonlinear oscillators and fractional oscillators, *J. Low. Freq. Noise V. A.*, **38** (2019), 1252–1260. https://doi.org/10.1177/1461348419844145
12. N. Qie, W. F. Houa, J. H. He, The fastest insight into the large amplitude vibration of a string, *Rep. Mech. Eng.*, **2** (2020), 1–5. https://doi.org/10.31181/rme200102001q
13. J. H. He, Q. Yang, C. H. He, Y. Khan, A simple frequency formulation for the tangent oscillator, *Axioms*, **10** (2021), 320. https://doi.org/10.3390/axioms10040320
14. C. H. He, C. Liu, A modified frequency-amplitude formulation for fractal vibration systems, *Fractals*, **30** (2022), 2250046. https://doi.org/10.1142/S0218348X22500463
15. Y. A. Amer, A. T. EL-Sayed, M. N. Abd El-Salam, A suitable active control for suppression of the vibrations of a cantilever beam, *Sound Vib.*, **56** (2022), 89–105. https://doi.org/10.32604/sv.2022.011838

16. H. S. Bauomy, A. T. EL-Sayed, A nonlinear time delay control influence in simulation aircraft tail contain a vertical cantilever beam, *Phys. Scr.*, **97** (2022), 085219. https://doi.org/10.1088/1402-4896/ac824c
17. O. Ekici, H. Boyaci, Effects of non-ideal boundary conditions on vibrations of microbeams, *J. Vib. Control*, **13** (2007), 1369–1378. https://doi.org/10.1177/1077546307077453
18. Y. A. Amer, R. E. Abdullah, O. M. Khaled, A. M. S. Mahdy, M. N. Abd El-Salam, Vibration control of smooth and discontinuous oscillator via negative derivative feedback, *J. Vib. Eng. Technol.*, **12 (**2024**)**, 2351–2363. https://doi.org/10.1007/s42417-024-01539-1
19. H. S. Bauomy, A. T. EL-Sayed, Safety of a quarter-vehicle car through negative derivative feedback controller, *Chaos Soliton. Fract.*, **166** (2023), 112960. https://doi.org/10.1016/j.chaos.2022.112960
20. R. Jamshidi, C. Collette, Designing negative derivative feedback controller based on maximum damping and H_2 method, *Smart Mater. Struct.*, **31** (2022), 075023. https://doi.org/10.1088/1361-665X/ac7682
21. F. Ripamonti, F. Cola, Control system for a carbon fiber plate using an adaptive negative derivative feedback control algorithm, *J. Vib. Control.*, **24** (2018), 4988–4999. https://doi.org/10.1177/1077546317740451
22. R. Jamshidi, A. A. Jafari , Conical shell vibration control with distributed piezoelectric sensor and actuator layer, *Compos. Struct.*, **256** (2021), 113107. https://doi.org/10.1016/j.compstruct.2020.113107
23. R. Jamshidi, A. A. Jafari, Nonlinear vibration of conical shell with a piezoelectric sensor patch and a piezoelectric actuator patch, *J. Vib. Control*, **28** (2022), 1502–1519. https://doi.org/10.1177/1077546321996922
24. R. Jamshidi, A. A. Jafari, Conical shell vibration optimal control with distributed piezoelectric sensor and actuator layers, *ISA T.*, **117** (2021), 96–117. https://doi.org/10.1016/j.isatra.2021.01.037
25. R. Jamshidi, A. A. Jafari, Evaluating sensor distribution in simply supported truncated conical shells with piezoelectric layers, *Mech. Adv. Mater. Struct.*, **26** (2019), 1179–1194. https://doi.org/10.1080/15376494.2018.1432791
26. R. Jamshidi, A. A. Jafari, Transverse sensing of simply supported truncated conical shells, *J Comput. Appl. Mech.*, **49** (2018), 212–230. https://doi.org/10.22059/JCAMECH.2017.238393.167
27. R. Jamshidi, A. A. Jafari. Evaluating actuator distributions in simply supported truncated thin conical shell with embedded piezoelectric layers, *J. Intell. Mater. Syst. Struct.*, **29** (2018), 2641–2659. https://doi.org/10.1177/1045389X18770905
28. B. Bao, D. Guyomar, M. Lallart, Vibration reduction for smart periodic structures via periodic piezoelectric arrays with nonlinear interleaved-switched electronic networks, *Mech. Syst. Signal Process.*, **82** (2017), 230–259. https://doi.org/10.1016/j.ymssp.2016.05.021
29. O. Thomas, J. Ducarne, J. F. Deü, Performance of piezoelectric shunts for vibration reduction, *Smart Mater. Struct.,* **21** (2011), 01500. https://doi.org/10.1088/0964-1726/21/1/015008
30. H. S. Bauomy, A. T. EL-Sayed, F. T. El-Bahrawy, Integral resonant negative derivative feedback suppression control strategy for nonlinear dynamic vibration behavior model, *Chaos Soliton. Fract.*, **189** (2024), 115686. https://doi.org/10.1016/j.chaos.2024.115686

31. K. Alluhydan, A. T. EL-Sayed, F. T. El-Bahrawy, The effect of proportional, proportional-integral, and proportional-integral-derivative controllers on improving the performance of torsional vibrations on a dynamical system, *Computation*, **12** (2024), 157. https://doi.org/10.3390/computation12080157
32. H. Bauomy, A. T. EL-Sayed, A. M. Salem, F. T. El-Bahrawy, The improved giant magnetostrictive actuator oscillations via positive position feedback damper, *AIMS Math.*, **8** (2023), 16864–16886. https://doi.org/10.3934/math.2023862
33. L. Grzegorz, M. Jerzy, G. Damian, Y. Daniil, D. Krzysztof, Dynamic response of the spherical pendulum subjected to horizontal Lissajous excitation, *Nonlinear Dyn.*, **102** (2020), 2125–2142. https://doi.org/10.1007/s11071-020-06023-5
34. B. Koch, R. Leven, Subharmonic and homoclinic bifurcations in a parametrically forced pendulum, *Physica D*, **16** (1985), 1–13. https://doi.org/10.1016/0167-2789(85)90082-X
35. Y. Guo, Albert C. J. Luo, Bifurcation trees of periodic motions in a parametrically excited pendulum, In: *ASME International Design Engineering Technical Conferences and Computers and Information in Engineering Conference*, 2017. https://doi.org/10.1115/DETC2017-67161
36. G. M. Moatimid, T. S. Amer, Dynamical system of time-delayed φ^6-Van der Pole oscillator: A non-perturbative approach, *Sci. Rep.*, **13** (2023), 11942. https://doi.org/10.1038/s41598-023-38679-5
37. G. M. Moatimid, A. T. El-Sayed, H. F. Salman, Different controllers for suppressing oscillations of a hybrid oscillator via non-perturbative analysis, *Sci. Rep.*, **14** (2024) 307. https://doi.org/10.1038/s41598-023-50750-9
38. G. M. Moatimid, M. A. A. Mohamed, K. Elagamy, An innovative approach in inspecting a damped Mathieu cubic–quintic Duffing oscillator, *J. Vib. Eng. Technol.*, **12** (2024), 1831–1848. https://doi.org/10.1007/s42417-024-01506-w
39. G. M. Moatimid, M. A. A. Mohamed, K. Elagamy, Insightful examination of some nonlinear classifications linked with Mathieu oscillators, *J. Vib. Eng. Technol.*, **13** (2025), 173. https://doi.org/10.1007/s42417-024-01688-3
40. G. M. Ismail, G. M. Moatimid, I. Alraddadi, S. V. Kontomaris, Scrutinizing highly nonlinear oscillators using He's frequency formula, *Sound Vib.*, **59** (2025), 2358. https://doi.org/10.59400/sv2358
41. A. Alanazy, G. M. Moatimid, M. A. A. Mohamed, Innovative methodology in scrutinizing nonlinear rolling ship in longitudinal waves, *Ocean Eng.*, **327** (2025), 120924, https://doi.org/10.1016/j.oceaneng.2025.120924
42. G. M. Moatimid, A. F. El-Bassiouny, M. A. A, Mohamed, Novel approach in inspecting nonlinear rolling ship in longitudinal waves, *Ocean Eng.*, **327** (2025), 120975, https://doi.org/10.1016/j.oceaneng.2025.120975
43. S. S. Mahmoud, A. EL-Sayed, S. Abd EL-Salam, IRC controller for suppressing the vibrations of cantilever beam excited by an external force, *Bulletin Fac. Sci.*, **2024** (2024), 131–139.
44. A. H. Nayfeh, *Perturbation methods*, New York: Wiley, 2000. https://doi.org/10.1002/9783527617609

45. C. Liu, X. Yue, Z. Yang, Are nonfragile controllers always better than fragile controllers in attitude control performance of post-capture flexible spacecraft? *Aerosp. Sci. Technol.*, **118** (2021), 107053. https://doi.org/10.1016/j.ast.2021.107053
46. B. Lyu, C. Liu, X. Yue, Integrated predictor-observer feedback control for vibration mitigation of large-scale spacecraft with unbounded input time delay, *IEEE T. Aero. Elec. Sys.*, **61** (2025), 4561–4572. https://doi.org/10.1109/TAES.2024.3505851

AIMS Press